WILEY-VCH

Ultralight Electrospun Composite Filters with Vertical Ternary Spatial Network for High-performance $PM_{0.3}$ Purification

Mengjuan Zhou[a,b,d], *Songlin Zhang*[c,*], *Hongyu Guo*[c], *Xinchang Zhou*[e], *Jinhao Xu*[d], *Qingliang Luo*[a], *Xiangshun Li*[a], *Qingli Xu*[f], *Chengdong Xiong*[a], *Rongwu Wang*[a], *Jintu Fan*[d,*], *Xiaohong Qin*[a,*], *Swee Ching Tan*[b,*]

M. Zhou, Q. Luo, X. Li, C. Xiong, R. Wang, X. Qin
Key Laboratory of Textile Science & Technology, Ministry of Education, College of Textiles
Donghua University
Shanghai 201620, China
E-mail: xhqin@dhu.edu.cn

M. Zhou, S. C. Tan
Department of Materials Science and Engineering, College of Design and Engineering
National University of Singapore, 117574, Singapore
E-mail: msetansc@nus.edu.sg

S. Zhang, H. Guo
Institute of Fibre Materials and Devices, Department of Macromolecular Science, State Key Laboratory of Molecular Engineering of Polymers
Fudan University
Shanghai 200438, China
E-mail: zhangsonglin@fudan.edu.cn

M. Zhou, J. Xu, J. Fan
School of Fashion and Textiles
The Hong Kong Polytechnic University
Hung Hom, Kowloon, 999077, Hong Kong, China
E-mail: jin-tu.fan@polyu.edu.hk

X. Zhou
The Second School of Clinical Medicine, Guangzhou University of Chinese Medicine
Guangzhou 510006, China

Q. Xu
National Engineering Laboratory for Modern Silk, College of Textile and Clothing Engineering
Soochow University
Suzhou, 215127, China

Keywords: spatial network structure, electrospinning, nanofiber filters, air purification, personal protection

Abstract: Air pollutants, particularly highly permeable particulate matter (PM), threaten public health and environmental sustainability due to extensive filter media consumption. Existing melt-blown nonwoven filters struggle with $PM_{0.3}$ removal, energy consumption, and disposal burdens. Here, we report an ultralight composite filter with a vertical ternary spatial network (TSN) structure that saves ~98% of raw material usage and reduces fabrication time by 99.4%, while simultaneously achieving high-efficiency $PM_{0.3}$ removal (≥99.92%), eco-friendly regeneration (near-zero energy consumption), and enhanced wearing comfort (breathability >80 mm s^{-1}, infrared transmittance >85%). The TSN filter consists of a hybrid layer of microsphere (average diameter: ~1 μm)/superfine nanofibers (~20 nm) sandwiched between two nanofiber scaffolds (diameter: ~400 nm and ~100 nm). This arrangement offers high porosity (~85%), ultralow areal density (<1 g m^{-2}), low airflow resistance (<90 Pa), guaranteeing superb thermal comfort. Notably, utilizing scalable one-step free surface electrospinning technology, TSN mats can be mass-produced at a rate of 60 meters per hour (width of 1.6 meters), which is critical and verified for various applications including window screens, individual respiratory protectors, and dust collectors. This work provides a viable strategy for designing high-performance nanofiber filter media through structural regulation in a scalable, cost-effective, and sustainable way.

1. Introduction

Suspended particulate matter (PM), particularly those smaller than 0.3 μm ($PM_{0.3}$), readily absorbs toxins, bacteria, and viruses, posing serious health risks to humans, including carcinogenic, teratogenic, and mutational effects.[1] Melt-blown nonwoven filters are widely used in commercial respiratory protective gears for the passive trapping of PMs.[2] However, it faces substantial environmental challenges, including energy consumption, extensive consumption of non-renewable raw materials, and greenhouse gas emission during disposal. For example, during the past global pandemic, the heavy use of normal melt-blown nonwoven respirators has consumed more than 1000 tons of raw materials per day.[2d] Concomitantly, the disposal of these respirators has imposed a substantial burden on environmental sustainability. In addition, the micron-scale fiber diameter (1–20 μm) and relatively large pore size (20–40 μm) result in inadequate interception of $PM_{0.3,}$ with an insufficient filtration efficiency (η) of only 20–80% (classified as the G2 class according to the standard EN779: 2012).[3] Commonly,

increasing the basis weight (areal density of up to ~50 g m^{-2}) of melt-blown filters by combining multiple layers of mats (thickness >90 μm) can improve filtration efficiency to some extent, but it results in high airflow resistance (ΔP >200 Pa), bulkiness, and discomfort during wear or use.[4]

Nanofiber filters (diameters averaged ($d_{av.}$) at 100–800 nm), typically produced by electrospinning, display excellent filtration performance because of their large specific surface area and small pore size, resulting in superior filtration efficiency (>90%).[5] However, filters with nanofiber webs usually have dense matrix structures that increase the airflow resistance (ΔP >150 Pa), resulting in high energy costs in industrial filtration processing and discomfort for personal protectives[2d]. Previous approaches to reduce airflow resistance have focused on complex structural designs of the nanofibers themselves, including nanoprotrusions,[6] bead-like,[7] wrinkled,[8] and ribbon-like structures.[9] Regulated nanofiber morphologies and tedious preparation procedures are still barriers for scale-up applications considering the current production rate (0.1–1 g h^{-1}) of nanofiber webs via traditional electrospinning.[10] Alternatively, laminated structures with different layers of electrospun nanofiber webs (*e.g.*, binary structures[11] and dual-scale structures[12]) can maintain efficient particle capture capability but still exhibit high airflow resistance (>100 Pa), compromising wearable comfort, especially for medical workers.[13] Therefore, the development of high-performing filters (η >99.9% for $PM_{0.3}$ removal, ΔP <100 Pa) with significantly reduced material usage, recyclability, and low energy requirement remains lacking.

In this article, we report a composite filter with a vertical ternary spatial network (TSN) structure to address the aforementioned issues. The TSN filter includes a hybrid web of microspheres ($d_{av.}$: ~1 μm) and superfine nanofibers ($d_{av.}$: ~20 nm) as a stuffing layer that is sandwiched between two nanofiber matrix webs as scaffolding layers. Our TSN design, with enlarged interference voids, presents a fluffy structure and elongated internal aperture channels. The assembled TSN filter has an ultralight areal density (<1 g m^{-2}), high porosity (~85%), prominent breathability (~80 mm s^{-1}), rapid spreading and evaporation of liquid water, superb heat and moisture transmission, radiative cooling (infrared transmittance ~85%), and excellent mechanical strength (~8.0 MPa). Importantly, such a thin structure of the TSN filter achieves superior removal efficiency for $PM_{0.3}$ aerosols (99.92%) with a quality factor (Qf) >0.08 Pa^{-1} at an ultralow airflow resistance (ΔP <89 Pa), surpassing that of commercial melt-blown nonwoven filter media. More importantly, such high-performance TSN filters can be mass-produced at a rate of up to 60 m h^{-1} (width of 1.6 m) via scalable one-step free surface electrospinning technology. Owing to the ultralow areal density and high-throughput

production capability, our TSN design could save raw materials by ~98% compared with commercial melt-blown filters and improve the fabrication time by 99.4% compared with conventional electrospinning methods. Our high-performance TSN filters are verified for various applications, including window screens, individual respiratory protectors, and industrial dust collectors. Notably, TSN webs possess eco-friendly solubility and can be readily regenerated for new nanofiber webs (**Figure 1a**). This work provides a viable strategy for designing high-performance nanofiber filter media by structural regulation through production scalability and environmental sustainability.

2. Results and Discussion

2.1. Design of the ternary spatial network (TSN) structure

The TSN filter is meticulously constructed into 3D interconnected stacking layers with fluffy and porous structures (Figure 1b, c). This TSN filter consists of a hybrid web with superfine nanofibers ($d_{av.}$: ~20 nm) surrounded by microspheres ($d_{av.}$: ~1 μm) (Hρ, where ρ denotes the hybrid webs prepared with 5, 6, 7, or 8 wt% precursor solutions, respectively). The hybrid layer is sandwiched between two matrix webs (without the hybrid web, referred to as M_x/M_y), in which the average nanofiber diameter ranges from 100–400 nm (M_x represents nanofiber webs with different fiber diameters, *e.g.*, the M_{100} web has an average fiber diameter of ~100 nm). The resulting TSN samples are referred to as M_x/Hρ/M_y, including M_{200}/Hρ/M_{400}, M_{100}/Hρ/M_{400}, and M_{200}/Hρ/M_{100}. The matrix webs (M_x/M_y) form a percolation skeleton, ensuring the robust mechanical strength of the TSN filter. Moreover, the hybrid web (Hρ) is fluffy, which is critical for constructing the TSN structure. First, the uniformly distributed microspheres inside Hρ not only provide sufficient space for airflow passage but also extend the length of aperture channels, increasing the probability of aerosol collision. Second, the superfine nanofibers wrapped around the microspheres form an interconnected 3D network that possesses strong interfacial adhesion with aerosols while minimizing airflow resistance under the “slip effect”. This is attributed to the negligible drag force with air molecules because their diameters are less than λ_{air} (~66 nm). Generally, whether for melt-blown filters or electrospun nanofiber filters in the conventional single structure, aerosols are captured mainly via settling, direct interception, or inertial impaction. Either some particles escape, or the filter has a large pressure drop due to straight and large pores with small tortuosity (Figure 1b).[13b] Even though nanofiber filters designed with dual-scale structure maintain enhanced filtration efficiency, they possess high air resistance owing to small pore size and dense packing density. Notably, this unique TSN assembly creates a tortuous cavity in the vertical direction between the hybrid and matrix webs,

providing ample opportunities and numerous sites for $PM_{0.3}$ capture along the airflow channels (Figure 1c). Therefore, the hierarchical structure of our TSN filter guarantees high filtration efficiency (HEPA, >99.9%) while still maintaining ultralow airflow resistance (<100 Pa).

The TSN webs are fabricated continuously via a one-step free surface electrospinning apparatus equipped with multiple modules (Figure 1d). The continuous production rate can reach 60 m h^{-1} at a width of 1.6 m (Figure 1e). Each module is configured with a mushroom head-shaped spinneret. Here, we select polyacrylonitrile (PAN, a low-cost raw polymer commonly used in industry) as an example for demonstrating the TSN design. By tuning the solution concentration (5–16 wt%), supply rate, electrospinning voltage, and platform traversing rate, nanofiber assemblies are uniformly generated with different diameters or morphologies. For example, a hybrid web (Hρ) was prepared from a PAN solution in 5–8 wt% concentration, resulting in superfine nanofibers ($d_{av.}$: <66 nm) and microspheres ($d_{av.}$: ~1 μm). The matrix webs (M_x/M_y) were prepared from solutions of 10–16 wt%, resulting in nanofibers 100–800 nm in diameter. The subsequent stacked layer-by-layer webs from the three modules (abbreviated as M_x/Hρ/M_y (Figure 1f, Table S1)) are supported by a transporting polypropylene (PP) nonwoven substrate. Consequently, the cost-effective manufacturing process, with the flexible tunability of the structural design, greatly enhances the practical usability and scalability of high-performance nanofiber filters.

Our TSN filter guarantees superior filtration performance for $PM_{0.3}$ to commercial melt-blown nonwoven filters and conventional-structure electrospun nanofiber filters (Figure 1g). Notably, it can dissolve promptly in solvents without emitting CO_2 in the ambient atmosphere and regenerate new nanofiber webs through electrospinning (Figure S1 and S2, Movie S1). In contrast, melt-blown filters require substantial external energy for disposal (Supplementary Figure 3). Furthermore, the TSN filter results in significantly lower raw-polymer consumption (0.1 kg per 100 m^2), achieving a 98% reduction compared with melt-blown nonwoven filters (5 kg per 100 m^2) (Figure 1h). Additionally, its raw material cost (4.5 ¥ per 100 m^2) is merely 2.4% of that for melt-blown filters (190 ¥ per 100 m^2). Furthermore, the production time of the TSN filter is only 0.3 h g^{-1} per spinneret, which is just 0.06% of the time required for conventional electrospun nanofiber filters (50 h g^{-1}). Overall, considering comprehensive indices (feasibility, money cost, time cost, raw material consumption, and greenhouse gas (CO_2) emission during postprocessing waste), our TSN filter emerges as a more efficient and sustainable solution for high-performing air pollutant purification (Figure 1i).

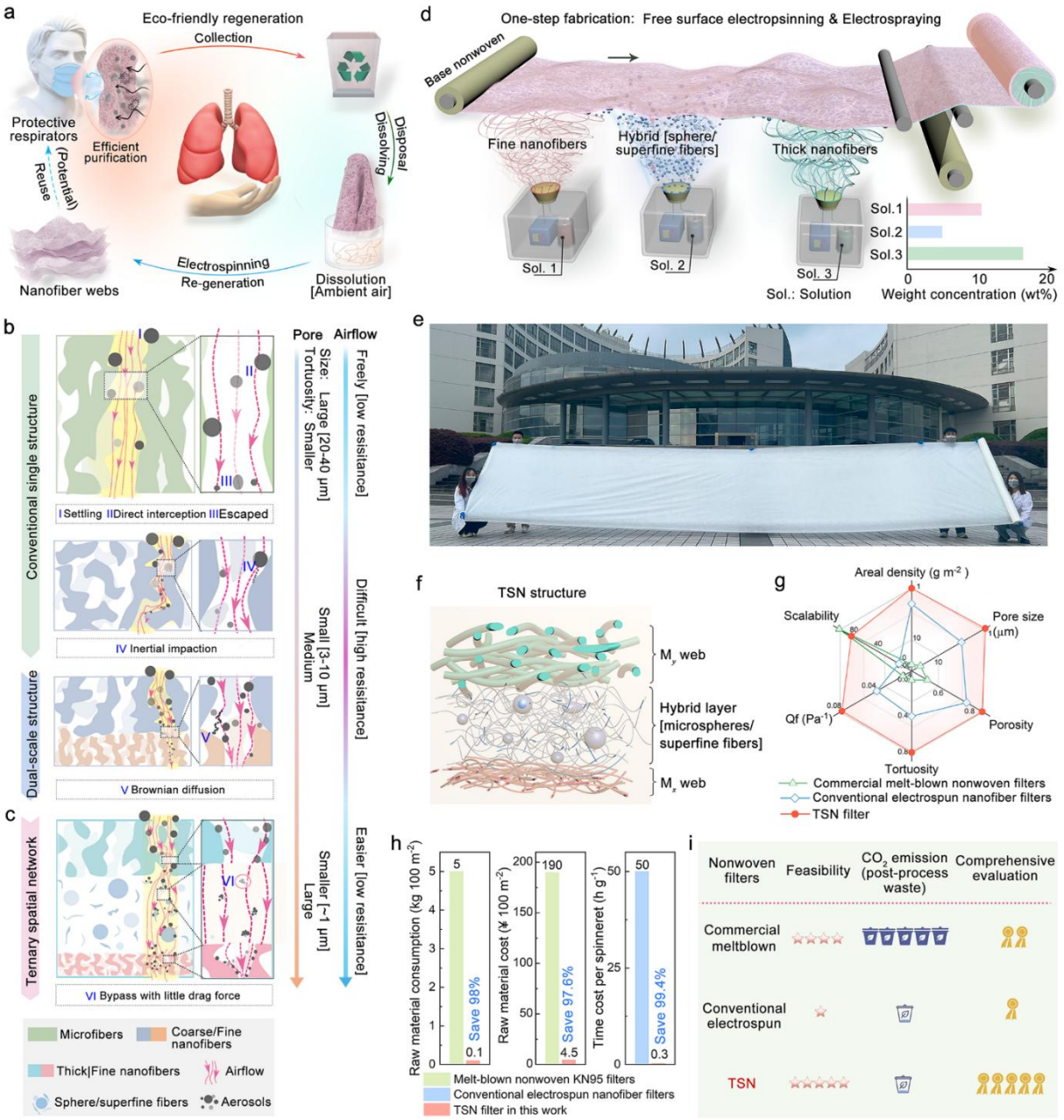

Figure 1. Fabrication of ternary spatial network (TSN) webs. a) Diagram of eco-friendly regeneration of nanofiber webs from disposal. Schematics of the distribution of aerosols captured by melt-blown nonwoven and electrospun nanofiber webs with conventional structures b) and the designed TSN structure c). d) Schematic of the fabrication of the TSN structure via one-step free surface electrospinning. e) Photographs of the TSN webs. f) Diagram of the 3D TSN structure. g) Performance comparisons of the TSN filter and conventional structural fiber filters. Raw material consumption and preparation costs h) and comparison of nonwoven filters i), including commercial melt-blown filters, conventional electrospun nanofiber webs, and our TSN filter.

2.2 Optimization of the TSN structure

The TSN webs, characterized by their fluffy properties, are perfectly integrated with an Hρ web sandwiched between M_x/M_y matrix webs. The Hρ web is critical for the construction of the TSN

structure. On the one hand, the Hρ hybrid (ρ = 5, 6, 7, and 8) is prepared from solutions with low weight concentrations (5–8 wt%), which is beneficial for the formation of microspheres as the skeleton surrounded by superfine nanofibers, resulting in high fluffiness. Briefly, the applied high-voltage electric field breaks the entangled polymer chains into fragments (a process known as "electrospraying") (**Figure 2a**).[10a] Consequently, a fluffy 3D honeycomb-like structure of the Hρ web is formed, where microspheres and discontinuous short superfine nanofibers are suspended slightly above each layer's surface owing to sufficient electrostatic charge[14]. On the other hand, when the solution concentration increases from 5 wt% to 8 wt%, the microspheres within the Hρ web grow longer and thinner, and their numbers decrease, whereas the diameter of the ultrafine nanofibers increases. This is attributed to the increased electrical conductivity and solution viscosity with increasing weight concentration (Figure S4). A further increase in the solution concentration (10–16 wt%) resulted in nanofibers with larger diameters, and the webs became more compact with decreased porosity (Figure 2b).

To construct a 3D interconnected tortuous cavity within TSN webs, gradient-structure matrix webs (M_x/M_y) are introduced. The Hρ webs are vertically integrated with two layers among the uniform M_{400}, M_{200}, and M_{100} webs (Figure 2c). The average fiber diameters of the M_{400}, M_{200}, and M_{100} webs are 420 nm, 200 nm, and 108 nm, respectively (Figure 2d). Additionally, the three M_x webs exhibit different surface topographies, with surface root mean square deviation (Sq) values of 0.743 μm, 0.234 μm, and 0.118 μm, respectively (Figure S5). The pore sizes of the M_{200}/M_{400}, M_{400}/M_{100}, and M_{100}/M_{200} webs are 1.73 μm (from M_{400} to M_{200})/1.07 μm (from M_{200} to M_{400}), 1.27 μm/0.94 μm, and 1.18 μm/0.97 μm, respectively (Figure 2e). Notably, the measured aperture channel sizes within the M_x/M_y webs decrease as airflow passes from the finer fiber side to the thicker side, which corresponds to their air permeability values (Figure S5). Moreover, as a critical component of the TSN webs, the Hρ web serves as an intermediate layer, uniformly constructed with microspheres and superfine nanofibers (Figure 2f). The number of generated microspheres decreases while the superfine nanofibers grow thicker as the mass concentrations of the precursor solutions increase (Figure 2g). For example, the H5 hybrid features nanobead strings ($d_{av.}$: 120 nm) with superfine nanofibers ($d_{av.}$: 16 nm) distributed evenly around the microsphere scaffold ($d_{av.}$: 0.9 μm), indicating optimal fluffiness. Ultimately, benefiting from both the fluffy Hρ and the flexible M_x/M_y, the TSN webs are uniquely integrated into a total of 15 combinations ($M_x/H\rho/M_y$, Figure 2h and Table S1). For example, $M_{100}/H5/M_{200}$ and $M_{100}/H5/M_{400}$ are well-architected and uniformly distributed across each layer (Figure 2i, j).

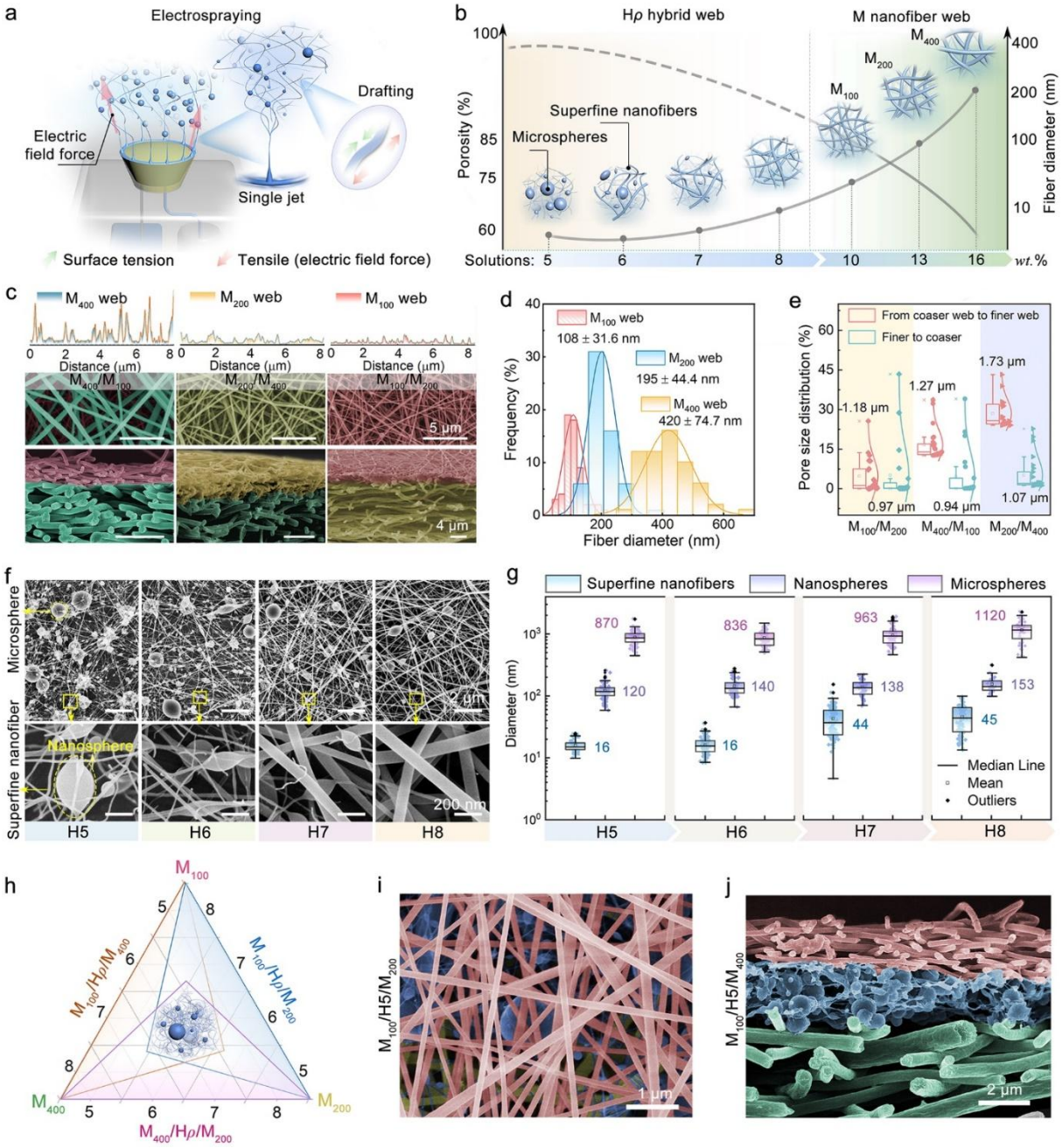

Figure 2. Structure of the TSN webs. Schematic diagrams of the electrospraying procedure a) and nanofiber webs with various structures b). c) SEM images of the surface and cross-section of the M_x/M_y webs. d) Fiber diameter distributions of the nanofibers. **e**, Pore size distributions of the M_x/M_y webs. SEM images f) and diameter distributions g) of Hρ webs. h) Demonstration of the integrated combinations for the TSN webs. SEM images of the surface of M_{100}/H5/M_{200} i) and the cross-section of M_{100}/H5/M_{400} j), respectively.

2.3 Characterizations

The properties of the TSN filters are systematically investigated (**Figure 3**). As one of the critical parameters, pore size plays a key role in the filtration performance of filter media. TSN webs, which are prepared with thicknesses of 4–8 μm and areal densities of 0.8–1.5 g m^{-2}, have internal pore sizes of less than 1 μm (Figure 3a, Figure S6). Among them, M_x/H7/M_y has a

smaller pore size (~0.6 μm) than M_x/H5/M_y (~0.8 μm). This is attributed to the H7 web containing a greater number of nanofibers, whereas the H5 web is mainly composed of microspheres and superfine nanofibers. Additionally, air permeability is a fundamental requirement for the comfort of filter media, especially for respiratory protectors. For the TSN webs, the larger the fiber diameter of the matrix webs, the higher the air permeability. For example, the M_{200}/Hρ/M_{400} webs have superior air permeability (~80 mm s^{-1}) compared with the other TSN webs (45–60 mm s^{-1}) (Figure 3b, Figure S7–9). Furthermore, mechanical strength is a vital indicator of the robustness of filter media, which is important in practical applications. For the TSN webs, the smaller the difference in fibre diameter between the matrix webs is, the better the mechanical properties. Specifically, the M_{100}/Hρ/M_{200} webs exhibit better breaking strength (8.30 MPa) than the M_{100}/Hρ/M_{400} webs do (<4 MPa) (Figure 3c, Figure S10). Additionally, the minimal structural difference between Hρ and the matrix webs contributes to the preferable fracture properties of the TSN webs. For example, M_{100}/H6/M_{200}, M_{100}/H7/M_{400}, and M_{200}/H8/M_{400} exhibit superior stress and strain properties, whereas M_x/H5/M_y shows suboptimal fracture properties.

Hydrophilicity is crucial for filter media, especially for respiratory protective equipment. The wettability of the TSN webs was investigated by measuring their advancing water contact angle (WCA). Structural integration with a high-porosity Hρ web alters the wettability of TSN webs, thereby facilitating water transmission. Briefly, the TSN webs become superhydrophilic (WCA: <40°), whereas the matrix webs (without the hybrid web) have WCA values of >75° (Figure 3d, e). For example, the M_{200}/M_{400} web is hydrophobic, with a WCA of 122° (Figure S11–13). Notably, the two sides of the TSN webs present dissimilar WCA values or water spreading rates because of their different structures (*i.e.*, pore size, surface roughness, *etc.*) (Supplementary Note 1). Comparatively, M_{200}/Hρ/M_{400} exhibits superior directional water transport properties (Figure S14). Furthermore, the water spreading process on both sides of the M_{100}/M_{200} web is demonstrated via COMSOL numerical simulation (Figure 3f). With the M_{200} layer (with a larger pore size and roughness) on top, the water droplet is rapidly pushed and penetrates the adjacent fibres and interferes with the pores. This is induced by the hydrostatic pressure (F_{HP}) and a large capillary force (F_C: 20.4 kPa). In contrast, when the water droplet contacts the M_{100} side (with a smaller pore size), it is only partially absorbed because of the lower F_C (1.92 kPa). Conversely, the F_C provided by the M_{200}/M_{400} web is negative, implying a hydrophobic force (F_{HF}). Thus, when water is applied upwards, it maintains a Wenzel–Cassie state, balancing the opposing forces (F_{HF} and F_{HP}). This observation is consistent with the experimental results showing the hydrophobicity of the M_{200}/M_{400} web.

The air purification performance of the TSN filters is evaluated for capturing $PM_{0.3}$. The TSN filters demonstrate both excellent filtration efficiency (>99.9%) and low airflow resistance (near or less than 100 Pa). Notably, TSN filters with different interlayered structures exhibit varying filtration performances. For example, $M_{100}/H\rho/M_{200}$ webs exhibit superior filtration efficiency (~99.98%) and air resistance (~140 Pa), with $M_{100}/H\rho/M_{400}$ webs close behind (Figure 3g). Particularly, $M_{200}/H\rho/M_{400}$ webs exhibit a superior Qf, thanks to their lowest air resistance, while maintaining comparable filtration efficiency to the other TSN filters ($M_{100}/H\rho/M_{200}$ and $M_{100}/H\rho/M_{400}$) (Figure 3h). For instance, $M_{200}/H5/M_{400}$ has a Qf as high as 0.08 Pa^{-1} (η: 99.92%, ΔP: 89 Pa). The excellent filtration performance of $M_{200}/H\rho/M_{400}$ webs can be attributed to the high filtration efficiency provided by the fluffy $H\rho$ web and the low air resistance offered by the two matrix webs (M_{200}/M_{400}) that possess large fiber diameters and pore sizes. Results indicated the integration of $H\rho$ with M_{200}/M_{400} matrix webs endows TSN filters with substantially enhanced filtration performance. Furthermore, among the TSN filters, $M_x/H5/M_y$ presents excellent performance because of the unique introduction of the fluffy H5 web. On the one hand, the uniformly distributed microspheres within the TSN structure effectively improve the interspace between matrix webs, facilitating smooth airflow transmission. On the other hand, the inlaid ultrafine nanofibers ($d_{av.}$: 16 nm, < λ_{air}) strongly adhere to aerosols along the streamlines with negligible drag force for air molecules under the "slip effect".[15] Apparently, particles are abundantly deposited on the windward side of the nanofiber surface, with no attachment on the leeward side (Figure 3i, Figure S15–17). Comparatively, the $M_{400}/H5/M_{200}$ web (areal density: 0.88 g m^{-2}) outperforms previously reported electrospun fibre filters[7, 16] and commercial filters, with superior removal efficiency (>99.92%) and ultralow air resistance (89 Pa) (Figure 3j, Table S2). Consequently, the exceptional filtration performance of TSN filters ensures their applicability in various practical scenarios.

To clearly illustrate the adsorption behavior of pollutants passing through the architecture, the internal partial skeleton is schematically represented in Figure 3k. The airflow regime surrounding an isolated cylinder is analyzed via the Knudsen number (K_n), which is estimated via Equation 1[13a]:

$$K_n = 2\lambda_{air}/d_f \quad (1)$$

where λ_{air} represents the mean free path of air molecules (~66 nm under ambient conditions) and d_f denotes the average fiber diameter. This equation encompasses four distinct flow regimes. A high K_n value indicates a low drag force on gas flowing around an isolated fiber. For the TSN webs, the K_n values are 0.3, 0.7, 1.2, and 8.3 for the individual fibers in the M_{400}, M_{200}, M_{100},

and Hρ webs, respectively. These values fall within the transition flow regime (0.25 <K_n <10), where air molecules can easily bypass the nanofibers with minimal drag force.[17] This perfectly explains the exceptional filtration performance of TSN filters, which exhibit both low air resistance and excellent separation efficiency.

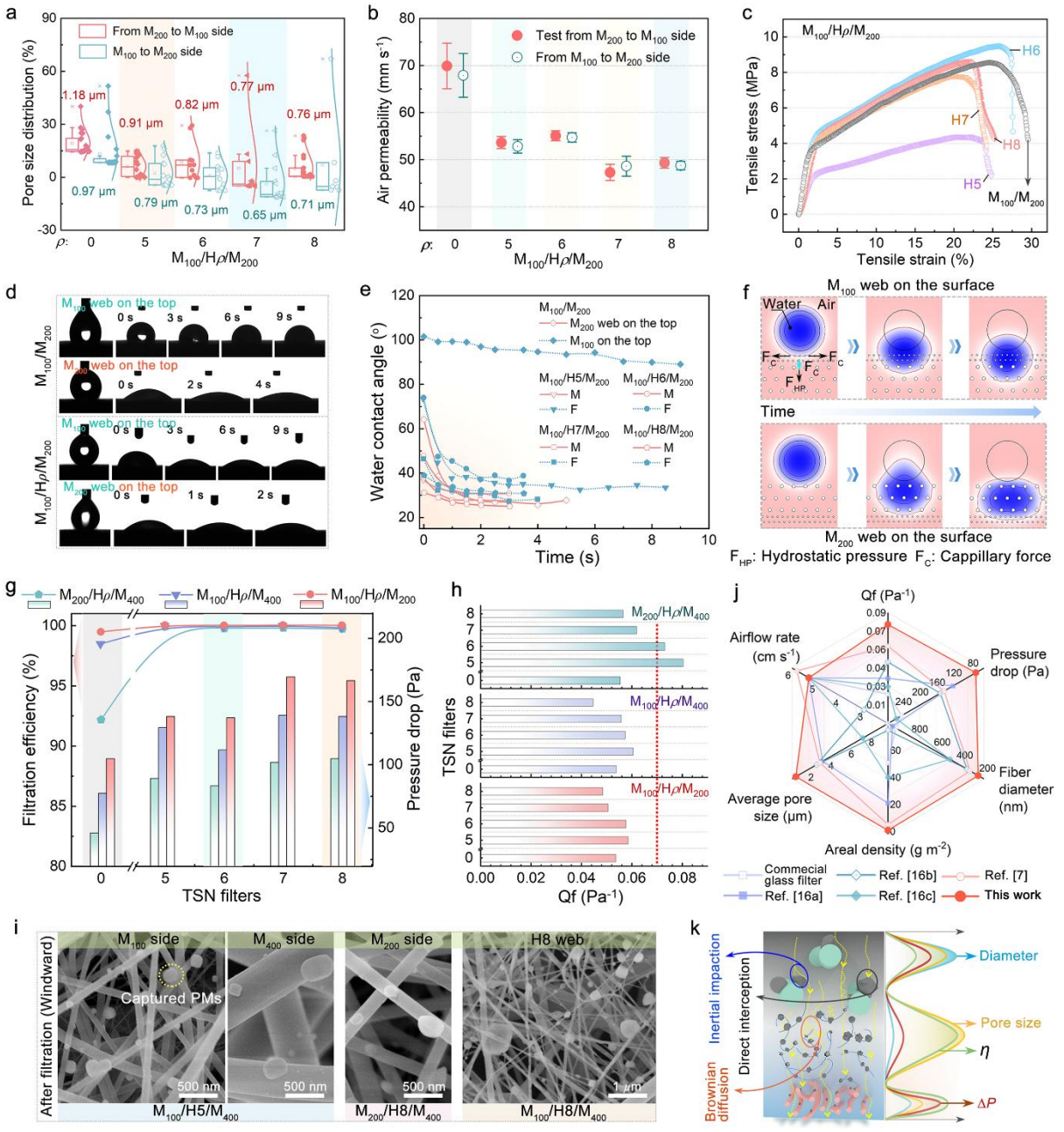

Figure 3. Performances of TSN filters. Pore size distribution a), air permeability b), and mechanical strength c) of TSN webs. d) Water transmission procedure for the double sides of M_{100}/M_{200} and $M_{100}/H5/M_{200}$ webs. e) Advancing water contact angles of $M_{100}/H\rho/M_{200}$. f) COMSOL numerical simulation of water transport around the two sides for M_{100}/M_{200}. Filtration efficiency/air resistance g) and Qf values h) and SEM images of the windward surface after air filtration i) for TSN filters. j) Performance comparisons of the TSN filter with previously reported nanofiber filters.[7, 16] k) Demonstration of PMs captured by $M_{400}/H\rho/M_{100}$.

2.4 Passive filtration modelling

The physical interception procedure of the TSN structure is further investigated via filtration modelling using COMSOL numerical simulation (**Figure 4**, Supplementary Note 2). Compared with other nanofibers, isolated nanofibers with smaller diameters interfere less with airflow, as evidenced by changes in the blue region area (Figure 4a).[18] However, the airflow trajectory significantly changes when it first encounters the fiber assembly vertically and then diminishes at the bottom (Figure 4b). According to Bernoulli's principle, air resistance is significant when airflow passes through a narrow orifice.[19] Under such restrictions, the flow rate of the fluid increases sharply, whereas the pressure decreases significantly. Additionally, in narrow channels, frictional resistance increases due to the relative increase in surface contact area (relative to the volume of the fluid) and higher flow rate. In the 3D TSN geometry, after bypassing the coarse nanofibers, airflow penetrates freely through the superfine nanofibers (~20 nm) at a slow speed, exiting from the bottom fine nanofibers (Figure 4c, d). Comparatively, airflow encounters the dense-structure 100 nm nanofiber assembly (d_f : 100 nm) with narrow aperture channels at a high speed. The results demonstrate the advantages of the TSN structure with extended aperture channels, facilitated by the inlaid high-porosity hybrid (microspheres and superfine nanofibers). Consequently, the TSN geometry results in a significantly lower pressure drop (223 Pa) than that of the 100 nm dense assembly (534 Pa), as indicated by the colour difference between the windward and leeward sides (Figure 4e). Furthermore, aerosols are effectively trapped around the TSN geometry (η: 87.8%), comparable to the 100 nm dense assembly (η: 92%) and significantly better than the 420 nm dense assembly (d_f: 420 nm) (η: 58.5%) (Figure 4f and g, Figure S18–20). The simulation results validate the advantages of the designed integrated TSN structure over conventional dense structures, offering both exceptional filtration efficiency and low air resistance. This provides valuable guidance for practical filtration implementations using the TSN structure.

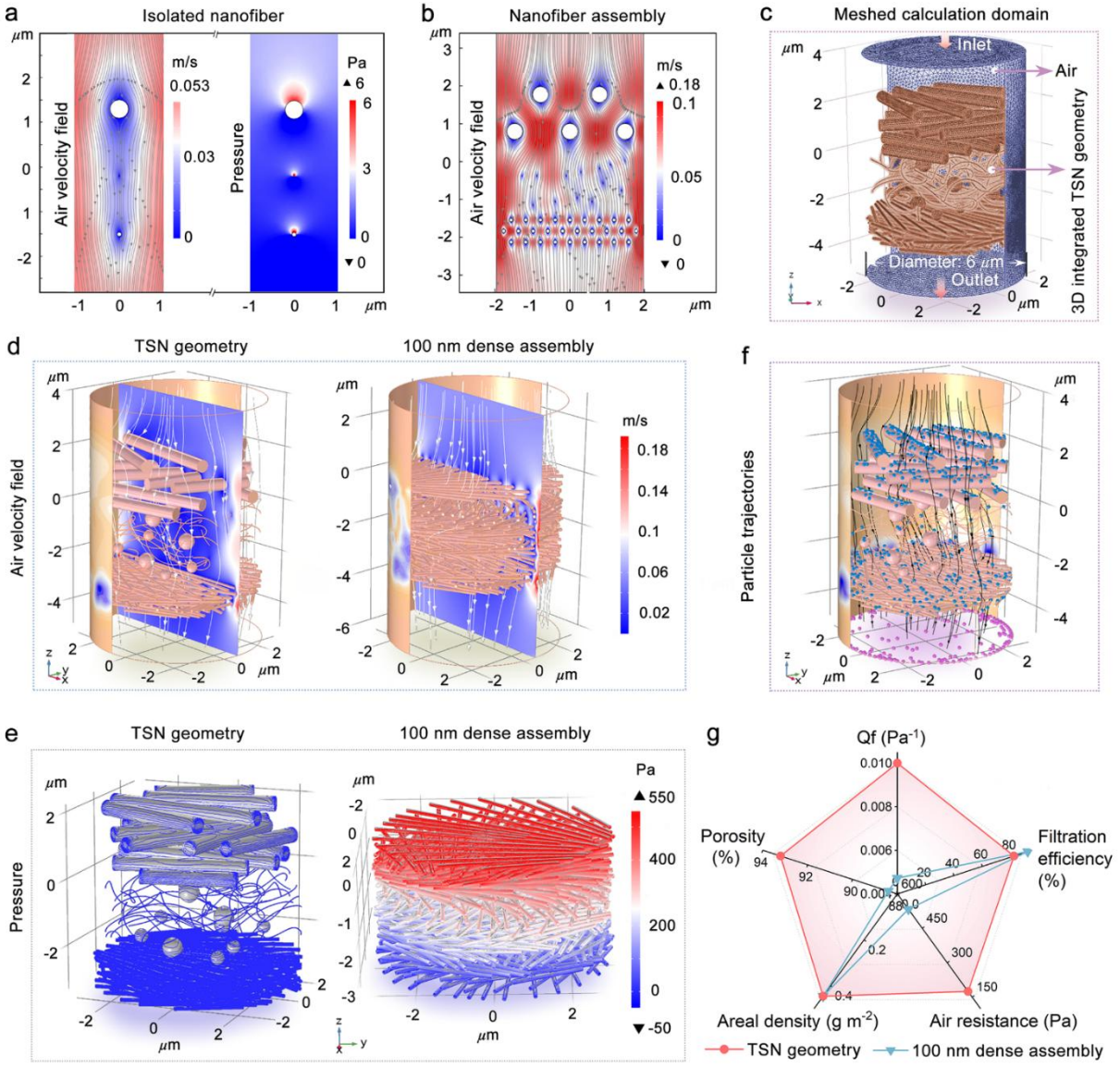

Figure 4. Simulation results of the filtration performance for the TSN structure. Numerical simulation results of the air velocity/pressure for a single nanofiber a) and multiple nanofibers b) of different sizes. c) Diagram of 3D integrated TSN geometry. Simulation results of the air velocity field d), pressure e), particle interception f), and properties g) for the TSN structure compared with those of the 100 nm dense assembly.

2.5 Filtration applications

The ultralight TSN filter is endowed with multiple functions, such as air purification, physiological thermal comfort, and antibacterial properties (**Figure 5a**). For demonstration, we simulate a severely polluted operational environment (*e.g.*, heavy haze days) via a custom-made setup (Figure 5b, Figure S21). During the dynamic filtration process, the TSN filter efficiently captures the generated PMs, with no pollutants escaping into the left bottle (remaining clear) (Movie S2). Consequently, the windward side of the sample darkens after filtration. Pollutant aggregations are anchored around the TSN web, with even distributions of external oxygen (O), chlorine (Cl), and sulfur (S). Furthermore, TSN filters can also exhibit exceptional antibacterial

properties when tiny amounts of antimicrobial agents (*e.g.*, amphiphilic dodecyl-trimethylammonium chloride (DTAC)) are doped into precursor solutions (Figure 5c). For example, when cultured on the TSN@DTAC website, both *Staphylococcus aureus* (*S. aureus*) and *Escherichia coli* (*E*. coli) are effectively killed. Their fatality rates reached 99% and 95%, respectively, in contrast to the good growth observed in the control groups (Figure S22, Supplementary Note 3).

To further demonstrate industrial applications, we develop a range of products using TSN filters, including face masks, window screens, and various core cartridges. Compared with commercial masks, the TSN filter-based face mask has superior heat and humidity transmission capabilities (Figure 5d). For example, during exhalation and inhalation, the surface temperature of the TSN-based mask (>30°C) is close to the body surface temperature, which is higher than that of the commercial mask (Figure S23). Additionally, the water on the skin surface is absorbed by the TSN filter and rapidly diffuses. This facilitates the evaporation of moisture into the external environment, unlike the hydrophobic commercial mask element. Furthermore, the TSN web provides superb radiative cooling properties by effectively transmitting radiation from the human body (infrared transmittance: ~85%) (Figure 5e). Moreover, TSN filter keep excellent filtration performance at high-humidity environment (Figure S24 and S25). These results indicate that the use of the TSN filter as an effective face mask provides excellent physiological thermal comfort. Furthermore, the TSN filter can be designed with ideal transparency in the visible light spectrum (transmittance: ~80%), highlighting its potential application as a window screen (Figure S26). Ultimately, the designed TSN webs are converted into a variety of filter media, including face shields, air purifiers, and window screens (Figure 5f). In particular, our TSN web exhibits rapid solubility in a solvent without generating CO_2 emissions (Movie S3). The resulting solution can be utilized for the regeneration of new nanofiber webs by electrospinning (see Figure 5j). This approach surpasses the disposal methods of commercial melt-blown nonwoven filters, such as landfills or incineration, which require additional time and energy and contribute to greenhouse gas emissions (Figure 5h).[20] This characteristic offers an effective solution for the substantial consumption of disposable filter media compared with commercial melt-blown nonwoven filters.

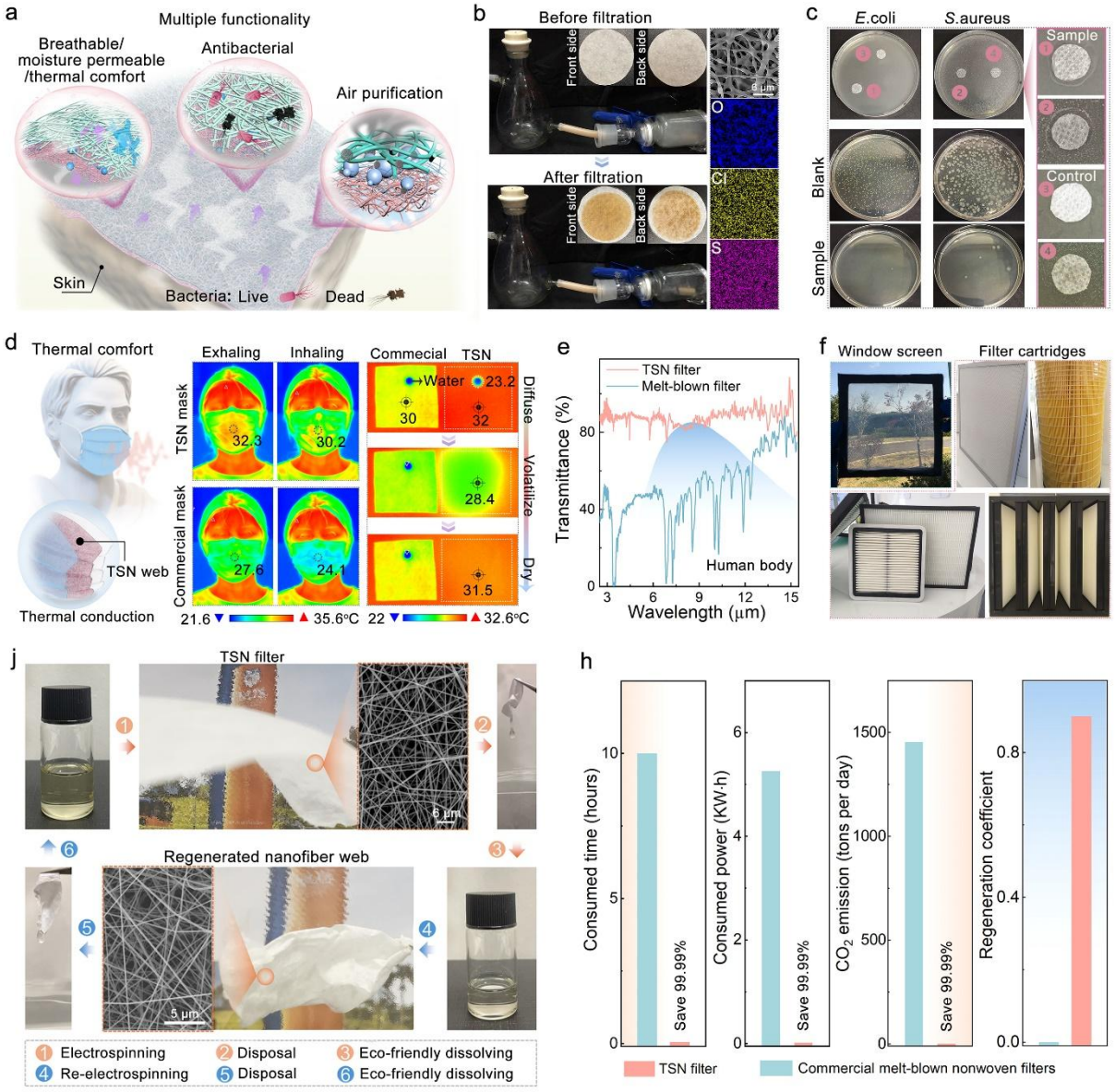

Figure 5. Applications of TSN filters. a) Diagram of a TSN material with multiple functions. b) Filtration scenario of the TSN filter for capturing PMs and mapping image of the windward side after filtration. c) Images of the inhibition zone and surviving bacteria under natural drying conditions after 24 h of treatment with the TSN material. d) IR images of exhaling and inhaling and water spreading on the surface of the TSN-based mask and commercial mask. e) Infrared transmittance of the TSN web. f) Photographs of the products applied to the TSN materials. j) Eco-friendly sustainability for TSN filter. h) Waste management of our TSN filters and melt-blown nonwoven filters (TSN webs dissolve promptly in solvents without emitting CO_2 in the ambient atmosphere, whereas melt-blown filters are not able to dissolve after being stirred at 80°C for 10 hours) and regenerate new nanofiber webs through electrospinning. For the daily consumption (1000 tons per day) of normal melt-blown respirators during the past global pandemic, the generated CO_2 emissions were equal to 1453 tons per day, which were calculated via formula[20] $E = W \times EF$, where W represents the burned waste mass and EF denotes the emission factor with a value of 1453 for CO^2).

3. Conclusion

In summary, we propose a composite nanofiber filter with a vertical ternary spatial network (TSN) structure for high-efficiency $PM_{0.3}$ removal, which is manifested by its feasible, cost-effective, and scalable production capability. The TSN structure perfectly integrates a hybrid web of microspheres ($d_{av.}$: ~1 μm) and superfine nanofibers ($d_{av.}$: ~20 nm) sandwiched between two nanofiber matrix webs. The TSN filter boasts an ultralight weight (<1 g m^{-2}), high porosity (~85%), excellent air permeability (~80 mm s^{-1}), good radiative cooling (infrared transmittance: ~85%), exceptional transparency (~80%), and decent mechanical properties (~8 MPa). Compared with commercial melt-blown nonwoven and other nanofiber filters, it delivers superior filtration performance (η: >99.9%, ΔP: <100 Pa), which is corroborated by both numerical simulations and experimental results. Our TSN filter can be mass-produced via a one-step continuous production line (60 m h^{-1}, width: 1.6 m). Compared with melt-blown nonwoven filters, our TSN design not only achieves an ~98% reduction in raw material consumption but also saves 99.4% of the fabrication time relative to conventional electrospun nanofiber filters. Additionally, high-performance TSN filters are ideal for applications in window screens, individual respiratory protectors with exceptional physiological thermal comfort, and industrial dust collector systems. In particular, the disposal of TSN filters can be readily value-added by the eco-friendly recycling of dissolution at room temperature and regenerated by electrospinning technology for new nanofiber webs. This work presents new insights into the design of high-performance nonwoven protective materials for personal respirators and other industrial dust collectors in a cost-effective and sustainable way.

4. Experimental Section

Materials: Polyacrylonitrile (PAN, M_w = 85,000) was obtained from the Shanghai Chemical Fibres Institute. *N*,*N*-Dimethylformamide (DMF, AR) and amphiphilic dodecyl-trimethylammonium chloride (DTAC) were supplied by Sinopharm Chemical Reagent Co., Ltd., China. The nonwoven polypropylene (PP) fabric substrate, characterized by a negligible filtration efficiency of 2% and a pressure drop of 5 Pa at an airflow velocity of 5.33 cm s^{-1}, was purchased from Nantong Yipinju Fabric Co., Ltd., China. All the chemicals were utilized as received without further purification.

Preparation of precursor solutions: PAN powder, which was dried under vacuum at 50°C for 4 hours, was dissolved in DMF and stirred via an electromechanical stirrer at 300 rpm in a water bath maintained at 70°C for 4 hours to prepare the PAN precursor solutions. The mass concentrations of the PAN solutions were 5, 6, 7, 8, 10, 13, and 16 wt%. The properties of these

solutions, including electrical conductivity, viscosity, and surface tension, were measured at ambient temperature and are presented in Figure S4.

Fabrication of the TSN filters: The compensating phase modular electrospinning apparatus, developed by our team[5a], facilitates seamless integration of the electrospinning process, from the feeding of the nonwoven fabric substrate to the winding of the final product (substrate/nanofiber webs/substrate), as illustrated in Figure 1d. This apparatus features multiple sets of electrospinning modules with free surface spinnerets, each with independent control and liquid supply systems. The nanofiber webs with hierarchical structures could be fabricated homogeneously via an electrospinning apparatus, which spans a width of 1.6 m at speeds ranging from 10 to 60 m h^{-1}.

The PAN nanofiber complex was fabricated via free surface electrospinning technology. PAN precursor solutions with weight concentrations of 10, 13, and 16 wt% were placed in modules No. 1 and No. 3 in three different combinations (10/13 wt%, 10/16 wt%, and 13/16 wt%), resulting in matrix webs (M_x/M_y) of the composite. The hybrid web, containing microspheres and superfine fibers, was fabricated via electrostatic spraying with low-concentration solutions (5~8 wt%) in module No. 2 (abbreviated as Hρ), which was sandwiched between the above matrix webs. The voltage applied to all precursor solutions was 55 kV, except for the 10 wt% PAN solution, which required 60 kV. The solution supply rates were 100 ml h^{-1} for Modules No. 1 and No. 3 and 80 ml h^{-1} for Module No. 2. The spinneret-to-collector distance was maintained at 20 cm, and the slide platforms moved forward and backwards at a speed of 9 m min^{-1} to ensure uniform nanofiber formation. The 10 wt% PAN solution produced nanofibers with an average diameter of ~100 nm, designated the M_{100} web. The fibers produced by the 13 wt% solution with an intermediate diameter of 200 nm were classified as the M_{200} web, and the nanofibers prepared via the 16 wt% solution, with an average diameter of 420 nm, were classified as the M_{400} web. Three combinations of the PAN complex were prepared: i) M_{100}/Hρ/M_{200}, ii) M_{100}/Hρ/M_{400}, and iii) M_{200}/Hρ/M_{400} (Table S1). For comparison, matrix webs composed of M_{100}, M_{200}, and M_{400} without a hybrid web (Hρ), including M_{100}/M_{200}, M_{100}/M_{400}, and M_{200}/M_{400}, were also prepared. As the PP nonwoven substrate traversed at a speed of 0.4 m min^{-1}, the PAN composite was deposited on the substrate, which was subsequently covered with PP nonwoven as a protective layer. The electrospinning process was conducted at 32 ± 5% relative humidity and 25 ± 3°C. After the composite was transferred to a drying device to ensure complete evaporation of the residual solvent, a 3D PAN composite material with a hierarchical structure (TSN) was successfully manufactured.

Characterizations: The properties of the precursor solutions, including viscosity, surface tension, and electrical conductivity, were measured via a rotary viscometer (DV3T, Brookfield Ltd., America), a surface tension meter (DCAT11, Data Physics Instrument Ltd., Germany), and a conductivity meter (Seven2Go, Mettler-Toledo Group, Switzerland), respectively. The surface morphology of the prepared fibrous webs was examined by scanning electron microscopy (SEM, TM3000, Hitachi Group, Japan) and field emission scanning electron microscopy (FESEM, SU8030, China). The diameter distribution of the submicron fibers was determined via Nano Measure 1.2 software by measuring 100 fibers. The basis weight and thickness of the prepared samples were determined via an electronic balance (MS105DU, Mettler-Toledo Group, Switzerland) and a thickness gauge (YG141N, Nantong Hongda Instruments Co., Ltd., China), respectively. The air permeability of the samples was assessed via a fully automatic permeability instrument (YG461G, Ningbo Spinning Instrument, China) at a test pressure of 100 Pa and a test area of 20 cm^2. The pore size distribution of the webs was characterized via a capillary flow porometer (POROLUXTM 100 FM, IB-FT Germany) with a pore volume of wetting fluid (surface tension of 16 mN m^{-1}). The mechanical properties of the samples were characterized by a fiber strength elongation tester (XQ-2, Shanghai Lipu Applied Science Institute, China). The fibrous web samples were cut into rectangular shapes with dimensions of 5 × 40 mm^2, clamped at the crosshead with a gauge length of 20 mm, and tested at a tensile speed of 10 mm min^{-1}. The porosity of the fibrous samples was calculated via the formula $p = (1 - D_{web}/D_{raw}) \times 100\%$, where D_{web} represents the bulk density of the materials and D_{raw} represents the skeletal density of the raw polymer used.

The filtration performance of the prepared fibrous materials was evaluated via an automated filtration testing machine (Model 8130, TSI Group, America). This machine delivers charge-neutralized monodisperse solid NaCl particles with a mass median diameter of 260 nm and a count median diameter of 75 nm. The NaCl particles passed through a filter with an effective area of 100 cm^2. All the filtration tests were conducted at room temperature under a continuous airflow face velocity of 5.33 cm s^{-1}, in accordance with the industrial testing standards specified by the USA standard (IEST-RP-CC52.2-2007) and the European standard (EN779: 2012). Three different fibrous samples were measured under the same conditions, and the average values were calculated. As a comprehensive evaluation indicator, the quality factor (Qf) was calculated via the formula $Qf = -\ln(1 - \eta)/\Delta P$, where η and ΔP represent the removal efficiency and pressure drop, respectively, both of which are automatically obtained from the machine. Additionally, a numerical simulation of the filtration performance of the constructed

structural fibrous filters was conducted via COMSOL Multiphysics software (Supplementary Note 2).

Statistical Analysis: All quantitative data were statistically analyzed and fitted using OriginPro 2018 unless otherwise stated. The data were presented and analyzed in original collected form.

Supporting Information

Supporting Information is available from the Wiley Online Library or from the author.

Acknowledgements

This work was partly supported by grant (52373032) from the National Natural Science Foundation of China, the International Cooperation Fund of Science and Technology Commission of Shanghai Municipality (21130750100), and the National Scholarship Council. Songlin Zhang acknowledges support from Fudan University (JIH2328001Y).

Received: ((will be filled in by the editorial staff))
Revised: ((will be filled in by the editorial staff))
Published online: ((will be filled in by the editorial staff))

References

[1] a) A. Seaton, D. Godden, W. MacNee, K. Donaldson, *Lancet* **1995**, 345, 176; b) Z. Zhang, D. Ji, H. He, S. Ramakrishna, *Mater. Sci. Eng. R Rep.* **2021**, 143, 100594; c) C. A. Pope, 3rd, D. W. Dockery, *J. Air Waste Manag. Assoc.* **2006**, 56, 709; d) Y. Xie, M. Zhou, K. M. R. Hunt, D. L. Mauzerall, *Nat. Sustain.* **2024**, 7, 983; e) C. C. Wang, K. A. Prather, J. Sznitman, J. L. Jimenez, S. S. Lakdawala, Z. Tufekci, L. C. Marr, *Science* **2021**, 373, eabd9149; f) S. K. Ravi, V. K. Singh, L. Suresh, C. Ku, V. Sanjairaj, D. K. Nandakumar, Y. Chen, W. Sun, P. H. Sit, S. C. Tan, *Small* **2020**, 16, e1906319.

[2] a) International Enviroguard, 2022; b) M. Zhou, L. Ma, Z. Zhou, Q. Xu, S. Zhang, Z. H. Guo, C. Xiong, W. Guo, R. Wang, S. C. Tan, X. Pu, X. Qin, *Nano Energy* **2024**, 121, 109230; c) Z. Zhong, Z. Xu, T. Sheng, J. Yao, W. Xing, Y. Wang, *ACS Appl. Mater. Interfaces* **2015**, 7, 21538; d) Y. Yang, X. Li, Z. Zhou, Q. Qiu, W. Chen, J. Huang, W. Cai, X. Qin, Y. Lai, *Nat. Commun.* **2024**, 15, 1586; e) M. Zhou, L. Shi, H. Dai, A. Obed, P. Liu, J. Wu, X. Qin, R. Wang, *Sep. Purif. Technol.* **2022**, 289, 120726.

[3] a) M. Li, Y. Feng, K. Wang, W. F. Yong, L. Yu, T. S. Chung, *Environ. Sci. Technol.* **2017**, 51, 10041; b) A. Damokhi, S. Yousefinejad, A. Fakherpour, M. Jahangiri, *J. Nanopart. Res.* **2022**, 24, 76.

[4] B. Y. Yeom, B. Pourdeyhimi, *J. Mater. Sci.* **2011**, 46, 5761.

[5] a) M. Zhou, M. Fang, Z. Quan, H. Zhang, X. Qin, R. Wang, J. Yu, *Environ. Sci. Nano* **2019**, 6, 3560; b) S. D. Skaria, G. C. Smaldone, *Ann. Occup. Hyg.* **2014**, 58, 771; c) S. Zhang, Y. Zhou, A. Libanori, Y. Deng, M. Liu, M. Zhou, H. Qu, X. Zhao, P. Zheng, Y.-L. Zhu, J. Chen, S. C. Tan, *Nat. Electron.* **2023**, 6, 338.

[6] Z. Niu, C. Xiao, J. Mo, L. Zhang, C. Chen, *ACS Appl. Mater. Interfaces* **2022**, 14, 27096.

[7] Z. Wang, C. Zhao, Z. Pan, *J. Colloid Interface Sci.* **2015**, 441, 121.

[8] a) X. Huang, T. Jiao, Q. Liu, L. Zhang, J. Zhou, B. Li, Q. Peng, *Sci. China Mater.* **2018**, 62, 423; b) R. Al-Attabi, Y. Morsi, W. Kujawski, L. Kong, J. A. Schütz, L. F. Dumée, *Sep. Purif. Technol.* **2019**, 215, 500.

[9] a) Y. Deng, T. Lu, X. Zhang, Z. Zeng, R. Tao, Q. Qu, Y. Zhang, M. Zhu, R. Xiong, C. Huang, *J. Membr. Sci.* **2022**, 660, 120857; b) Y. Zhang, Y. Han, X. Ji, D. Zang, L. Qiao, Z. Sheng, C. Wang, S. Wang, M. Wang, Y. Hou, X. Chen,

X. Hou, *Nature* **2022**, 610, 74; c) Q. Su, Z. Wei, C. Zhu, X. Wang, W. Zeng, S. Wang, S. Long, J. Yang, *J. Hazard Mater.* **2022**, 431, 128514; d) G. Yan, Z. Yang, J. Li, H. Li, J. Wei, L. Shi, Z. Li, J. Chen, L. Wang, Y. Wu, *Small* **2023**, 19, e2206403.

[10] a) H. Gao, Y. Yang, O. Akampumuza, J. Hou, H. Zhang, X. Qin, *Environ. Sci. Nano* **2017**, 4, 864; b) S. Zhang, M. Zhou, M. Liu, Z. H. Guo, H. Qu, W. Chen, S. C. Tan, *Nat. Commun.* **2023**, 14, 3245; c) V. K. Singh, S. K. Ravi, W. Sun, S. C. Tan, *Small* **2017**, 13.

[11] S. Zhang, H. Liu, X. Yin, J. Yu, B. Ding, *ACS Appl. Mater. Interfaces* **2016**, 8, 8086.

[12] J. Wang, W. Zhao, B. Wang, G. Pei, C. Li, *J. Appl. Polym. Sci.* **2017**, 134, 16.

[13] a) Z. Quan, Y. Zu, Y. Wang, M. Zhou, X. Qin, J. Yu, *Sep. Purif. Technol.* **2021**, 275, 119258; b) C. Liu, P. C. Hsu, H. W. Lee, M. Ye, G. Zheng, N. Liu, W. Li, Y. Cui, *Nat. Commun.* **2015**, 6, 6205; c) S. Zhang, H. Liu, X. Yin, Z. Li, J. Yu, B. Ding, *Sci. Rep.* **2017**, 7, 40550.

[14] J. M. Deitzel, J. Kleinmeyer, D. E. A. Harris, N. B. Tan, *Polymer* **2001**, 42, 261.

[15] S. Zhang, H. Liu, N. Tang, S. Zhou, J. Yu, B. Ding, *Adv. Mater.* **2020**, 32, e2002361.

[16] a) N. Wang, A. Raza, Y. Si, J. Yu, G. Sun, B. Ding, *J. Colloid Interface Sci.* **2013**, 398, 240; b) A. C. Canalli Bortolassi, V. G. Guerra, M. L. Aguiar, L. Soussan, D. Cornu, P. Miele, M. Bechelany, *Nanomaterials* **2019**, 9, 1740; c) M. A. Hassan, B. Y. Yeom, A. Wilkie, B. Pourdeyhimi, S. A. Khan, *J. Membr. Sci.* **2013**, 427, 336.

[17] C. Yang, *Chin. J.* Chem. *Eng.* **2012**, 20, 1.

[18] J. Wu, O. Akampumuza, P. Liu, Z. Quan, H. Zhang, X. Qin, R. Wang, J. Yu, *Materi. Today Commun.* **2020**, 23, 100897.

[19] a) H. Yang, M. V. Balakuntala, J. J. Quinones, U. Kaur, A. E. Moser, A. Doosttalab, A. Esquivel-Puentes, T. Purwar, L. Castillo, X. Ma, L. T. Zhang, R. M. Voyles, *Rob. Auton. Syst.* **2022**, 147, 103919; b) S. Castellano, G. Starace, L. De Pascalis, M. Lippolis, G. Scarascia-Mugnozza, *J. Agric. Eng.* **2016**, 47, 134.

[20] C. Wiedinmyer, R. J. Yokelson, B. K. Gullett, *Environ Sci Technol* **2014**, 48, 9523.

[21] T. Zhao, Y. Xu, M. Wu, Y. Li, J. Ma, H. Li, Y. Zheng, Y. Zeng, *Nano Lett* **2024**, 24, 1385.

Ultralight Electrospun Composite Filters with Vertical Ternary Spatial Network for High-performance $PM_{0.3}$ Purification

Mengjuan Zhou[a,b,d], Songlin Zhang[c,*], Hongyu Guo[c], Xinchang Zhou[e], Jinhao Xu[d], Qingliang Luo[a], Xiangshun Li[a], Qingli Xu[f], Chengdong Xiong[a], Rongwu Wang[a], Jintu Fan[d,*], Xiaohong Qin[a,*], Swee Ching Tan[b,*]

ToC Figure

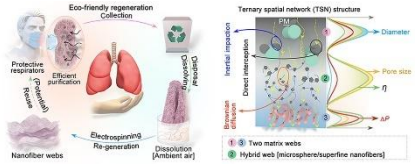

ToC text: An innovative ultralight electrospun nanofiber composite filter has been engineered with a vertical ternary spatial network (TSN) structure, featuring elongated internal aperture channels. This advanced TSN filter excels in high-efficiency filtration of ultrafine $PM_{0.3}$ aerosols while significantly minimizing material usage. It is designed for recyclability and operates with low energy requirements, ensuring both wearer comfort and environmental sustainability.

Supporting Information

Ultralight Electrospun Composite Filters with Vertical Ternary Spatial Network for High-performance $PM_{0.3}$ Purification

Mengjuan Zhou[a,b,d], *Songlin Zhang*[c,*], *Hongyu Guo*[c], *Xinchang Zhou*[e], *Jinhao Xu*[d], *Qingliang Luo*[a], *Xiangshun Li*[a], *Qingli Xu*[f], *Chengdong Xiong*[a], *Rongwu Wang*[a], *Jintu Fan*[d,*], *Xiaohong Qin*[a,*], *Swee Ching Tan*[b,*]

M. Zhou, Q. Luo, X. Li, C. Xiong, R. Wang, X. Qin
Key Laboratory of Textile Science & Technology, Ministry of Education, College of Textiles
Donghua University
Shanghai 201620, China
E-mail: xhqin@dhu.edu.cn

M. Zhou, S. C. Tan
Department of Materials Science and Engineering, College of Design and Engineering
National University of Singapore, 117574, Singapore
E-mail: msetansc@nus.edu.sg

S. Zhang, H. Guo
Institute of Fibre Materials and Devices, Department of Macromolecular Science, State Key Laboratory of Molecular Engineering of Polymers
Fudan University
Shanghai 200438, China
E-mail: zhangsonglin@fudan.edu.cn

M. Zhou, J. Xu, J. Fan
School of Fashion and Textiles
The Hong Kong Polytechnic University
Hung Hom, Kowloon, 999077, Hong Kong, China
E-mail: jin-tu.fan@polyu.edu.hk

X. Zhou
The Second School of Clinical Medicine, Guangzhou University of Chinese Medicine
Guangzhou 510006, China

Q. Xu
National Engineering Laboratory for Modern Silk, College of Textile and Clothing Engineering
Soochow University
Suzhou, 215127, China

Content

Supplementary Table 1. Preparation of PAN fibrous complex with different hierarchical structures.

Samples	No. 1 Module		No. 2 Module		No. 3 Module	
	Voltage (kV)	Solutions (wt%)	Voltage (kV)	Solutions (wt%)	Voltage (kV)	Solutions (wt%)
M_{100}/M_{200}	60	10	\	\	55	13
$M_{100}/H5/M_{200}$			55	5		
$M_{100}/H6/M_{200}$				6		
$M_{100}/H7/M_{200}$				7		
$M_{100}/H8/M_{200}$				8		
M_{100}/M_{400}	60	10	\	\	55	16
$M_{100}/H5/M_{400}$			55	5		
$M_{100}/H6/M_{400}$				6		
$M_{100}/H7/M_{400}$				7		
$M_{100}/H8/M_{400}$				8		
M_{200}/M_{400}	60	13	\	\	55	16
$M_{200}/H5/M_{400}$			55	5		
$M_{200}/H6/M_{400}$				6		
$M_{200}/H7/M_{400}$				7		
$M_{200}/H8/M_{400}$				8		

Supplementary Fig. 1 The procedure of TSN web waste dissolving in *N*,*N*-Dimethylformamide (DMF) at ambient atmosphere.

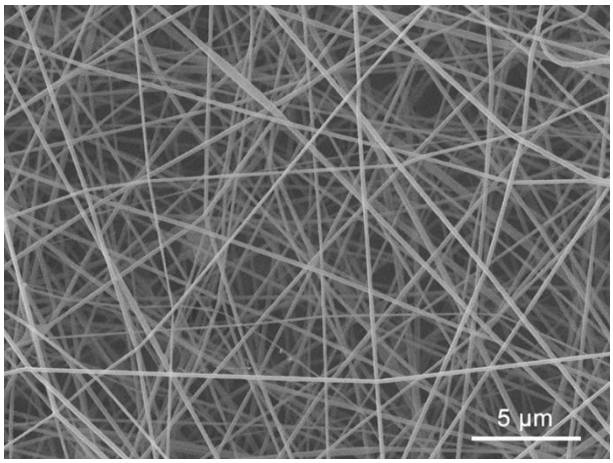

Supplementary Fig. 2 SEM image of the regenerated nanofiber web.

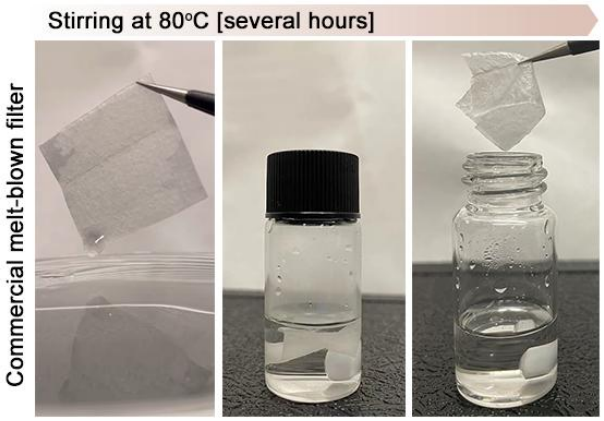

Supplementary Fig. 3 The dissolving procedure of commercial melt-blown nonwoven filter in DMF solvent after stirring at 80°C for several hours.

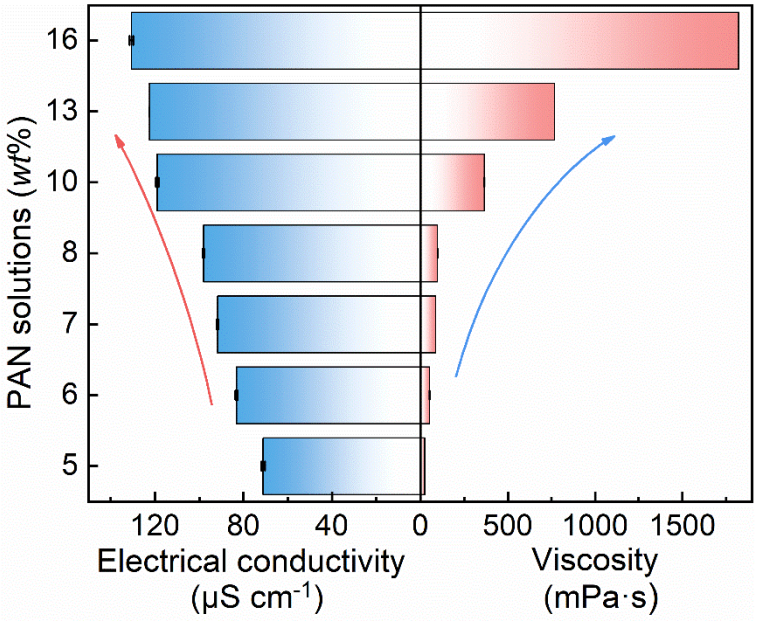

Supplementary Fig. 4 The properties of PAN solutions with different mass concentrations.

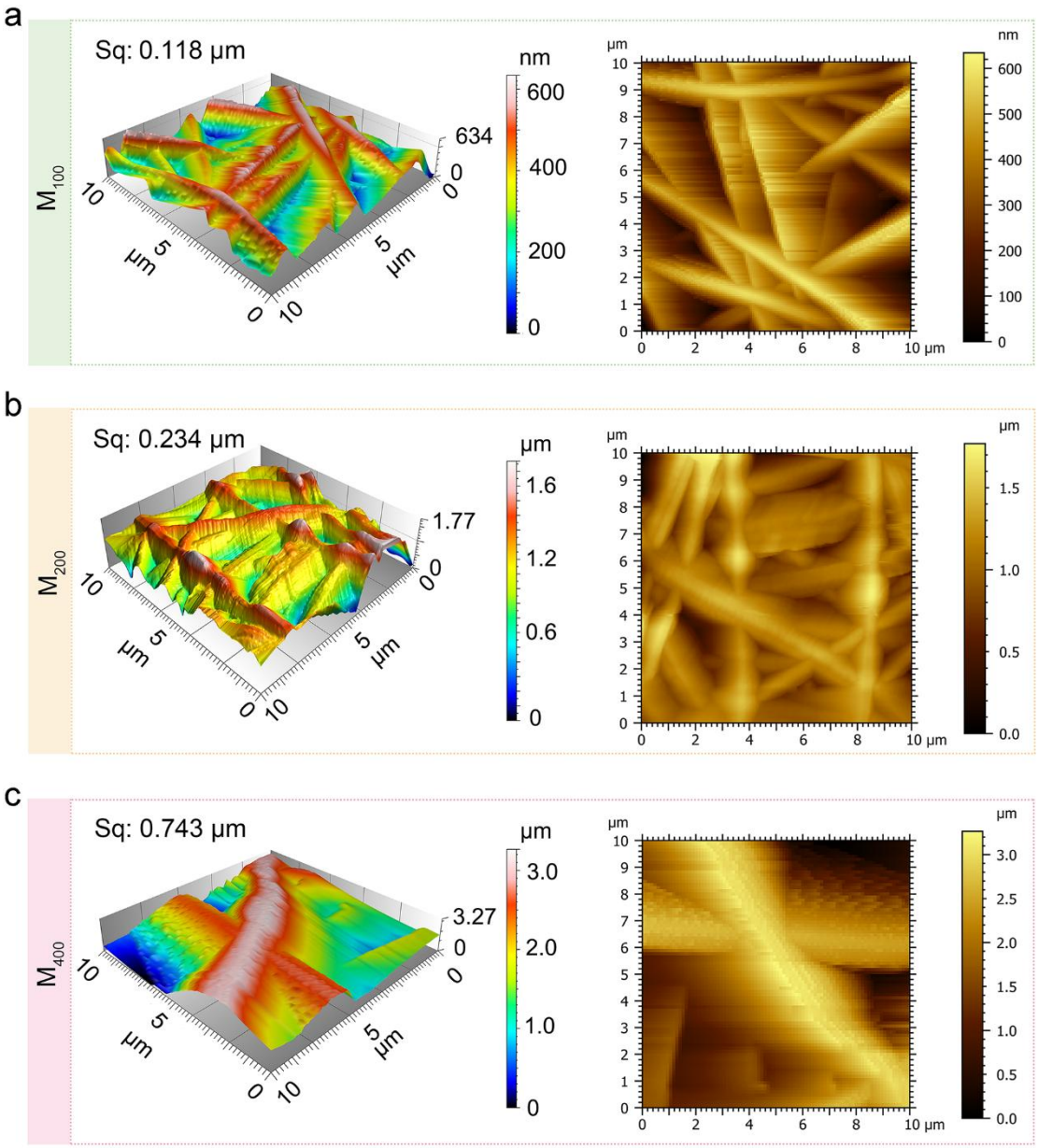

Supplementary Fig. 5 The 3-D pseudo color views of M100 (a), M200 (b), and M400 (c) webs.

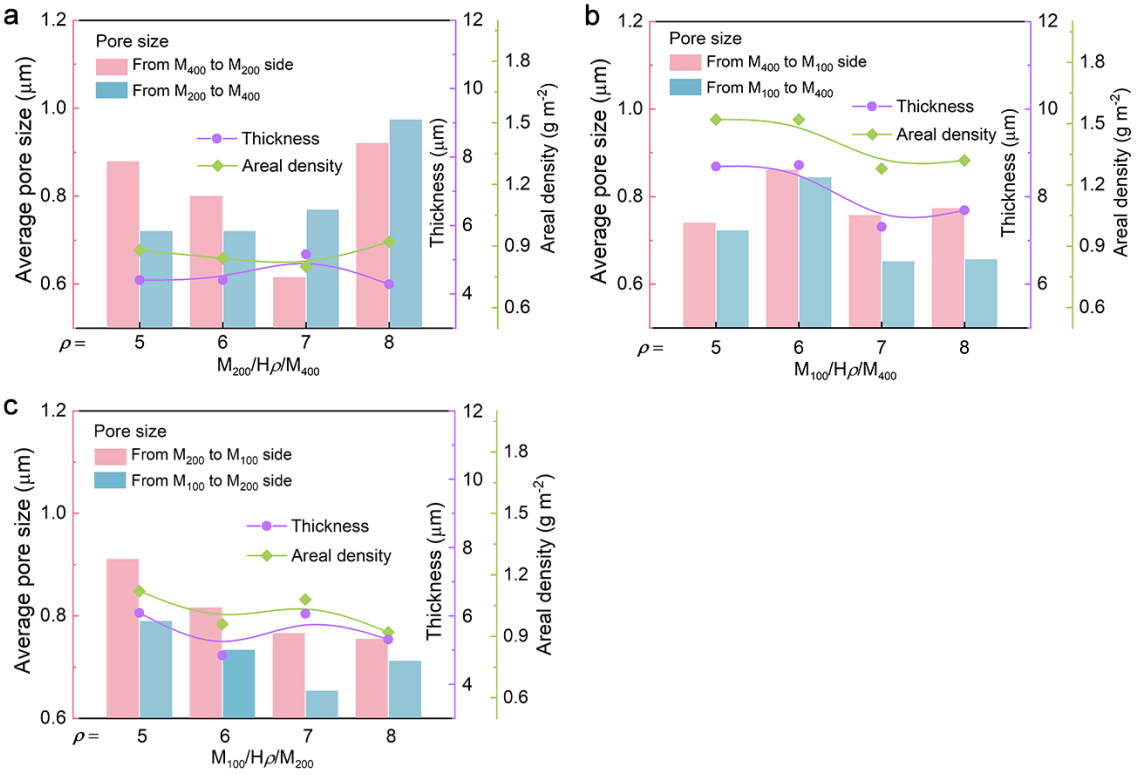

Supplementary Fig. 6 Average pore size, thickness, and areal density of $M_{100}/H\rho/M_{400}$ (a), $M_{200}/H\rho/M_{400}$ (b), and $M_{100}/H\rho/M_{200}$ (c).

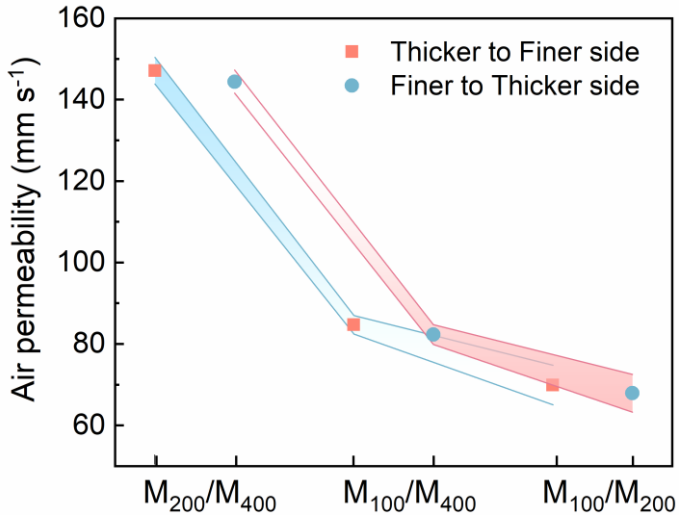

Supplementary Fig. 7 Air permeability of M_x/M_y webs.

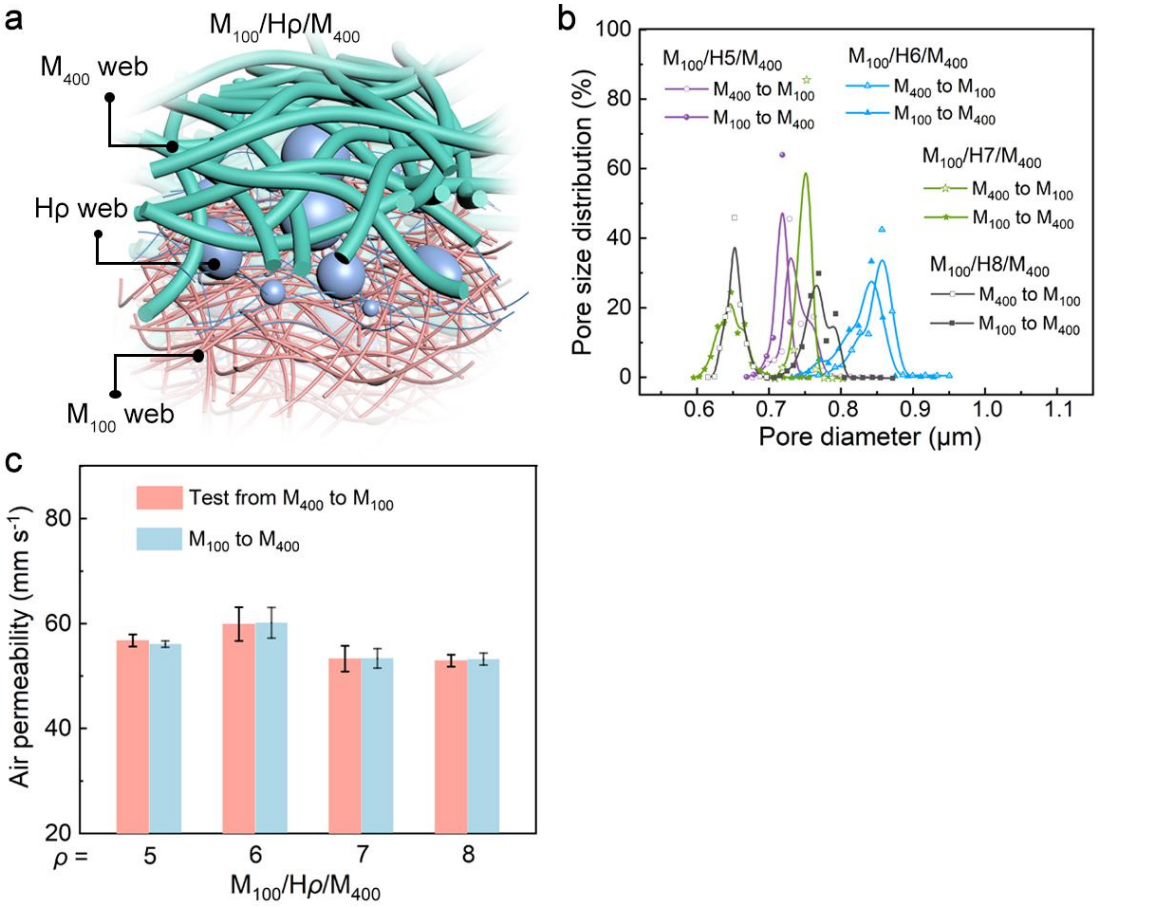

Supplementary Fig. 8 (a) Schematic diagram of structure, (b) pore size distribution, and (c) air permeability of $M_{100}/H\rho/M_{400}$.

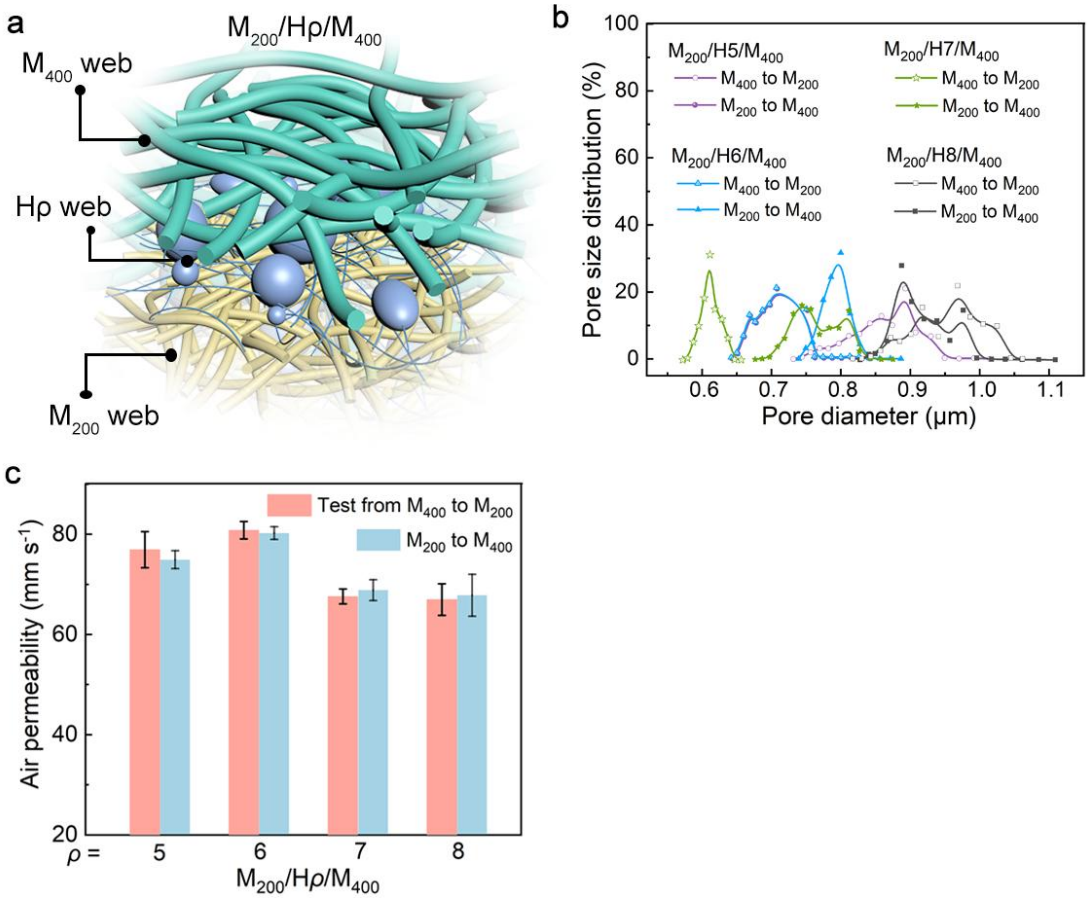

Supplementary Fig. 9 (a) Schematic diagram of structure, (b) pore size distribution, and (c) air permeability of $M_{200}/H\rho/M_{400}$.

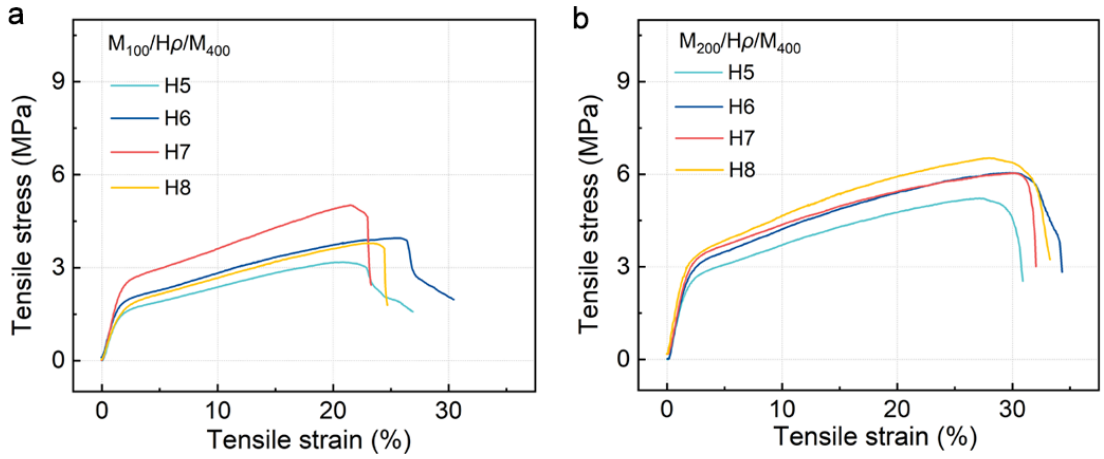

Supplementary Fig. 10 Tensile stress/strain curves of $M_{100}/H\rho/M_{400}$ (a) and $M_{200}/H\rho/M_{400}$ (b) webs.

Supplementary Note 1

Hydrophilicity of TSN webs

The water transport process through two matrix webs (M_x/M_y) has been specifically studied in depth, considering factors such as surface roughness, hydrostatic pressure, and pore size.[S1] Typically, when a water droplet contacts a material, it spreads through capillary channels under capillary force, as estimated via the Young–Laplace equation (Eq. S1):

$$P = 4\gamma \cdot cos\theta / D_{pore} \quad \text{(S1)}$$

where P is the Laplace pressure, γ represents the surface tension of liquid water, θ indicates the WCA of the capillary surface, and D_{pore} is the average pore diameter of the fibre webs.[S2] In the matrix webs, the two sides with different pore sizes exert different P values on the water droplet since P is inversely proportional to D_{pore}.

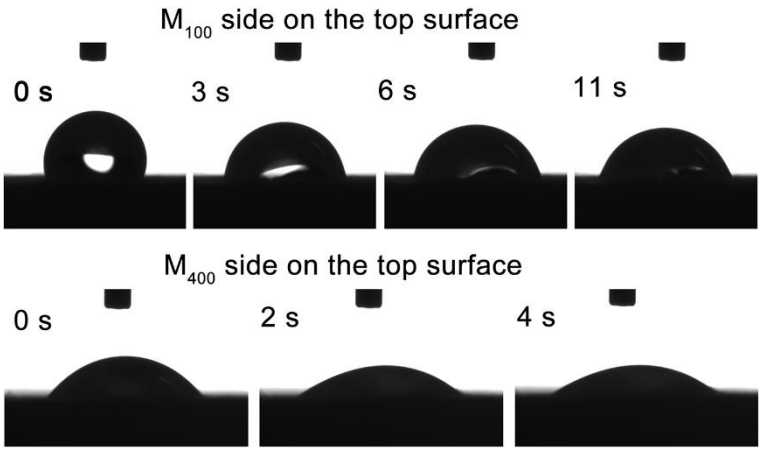

Supplementary Fig. 11 Apparent WCA for double sides of M_{100}/M_{400} web.

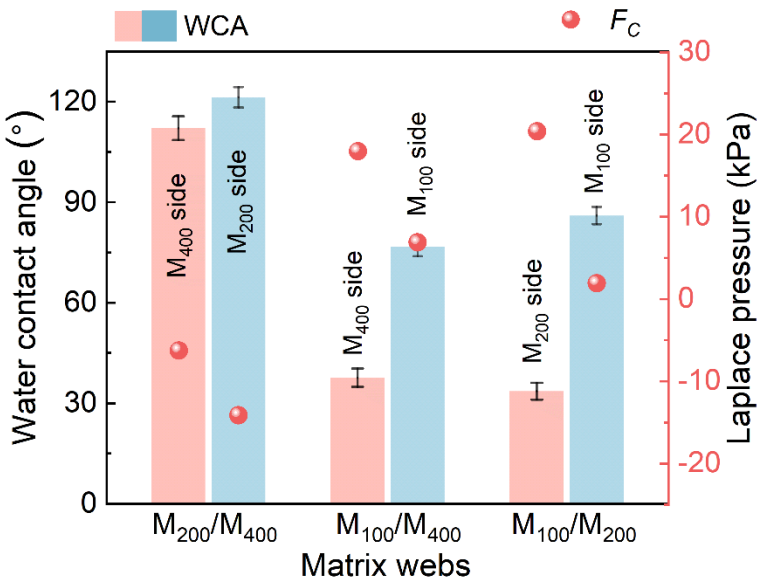

Supplementary Fig. 12 Water contact angles and Laplace pressure values of M_x/M_y matrix webs.

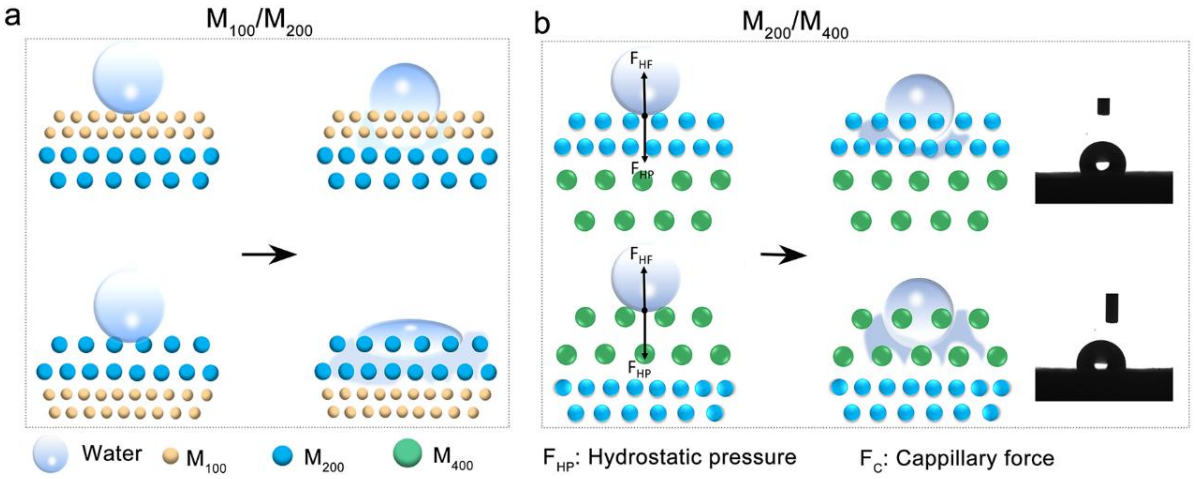

Supplementary Fig. 13 Schematic diagrams of the directional water transport mechanism for M_{100}/M_{200} (a) and M_{200}/M_{400} (b) webs.

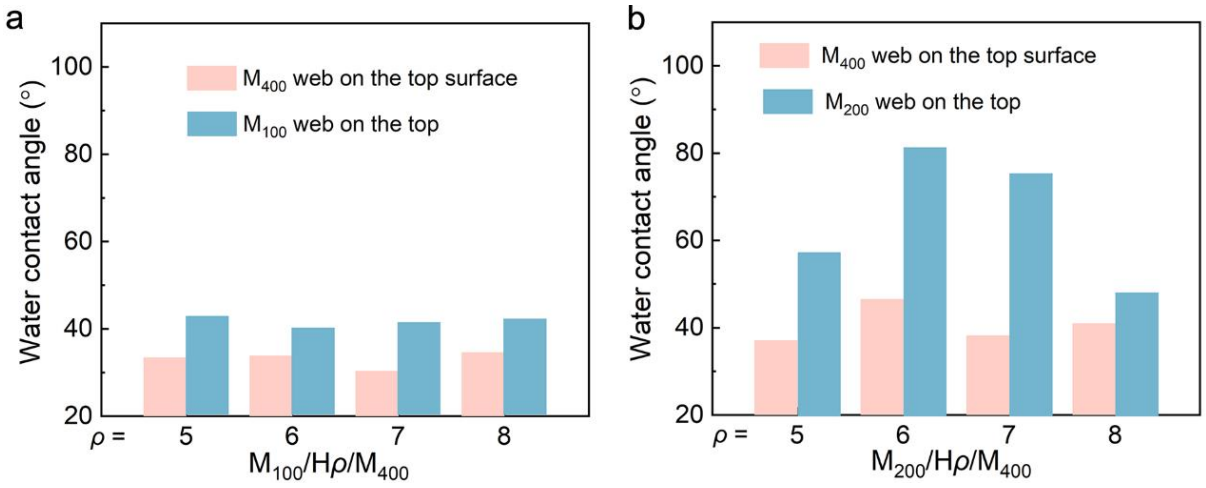

Supplementary Fig. 14 Water contact angles of $M_{100}/H\rho/M_{400}$ (a) and $M_{200}/H\rho/M_{400}$ (b) webs.

The WCA value on the M_{200} or M_{400} side of $M_{100}/H\rho/M_y$ is smaller than that on the M_{100} side. Similarly, the WCA value on the M_{200} side of $M_{200}/H\rho/M_{400}$ is smaller than that on the M_{400} side. The two sides of this web possess significantly different hydrophilicities, with the M_{400} side having a WCA value of ~40° and the M_{200} side having a WCA value of ~80°.

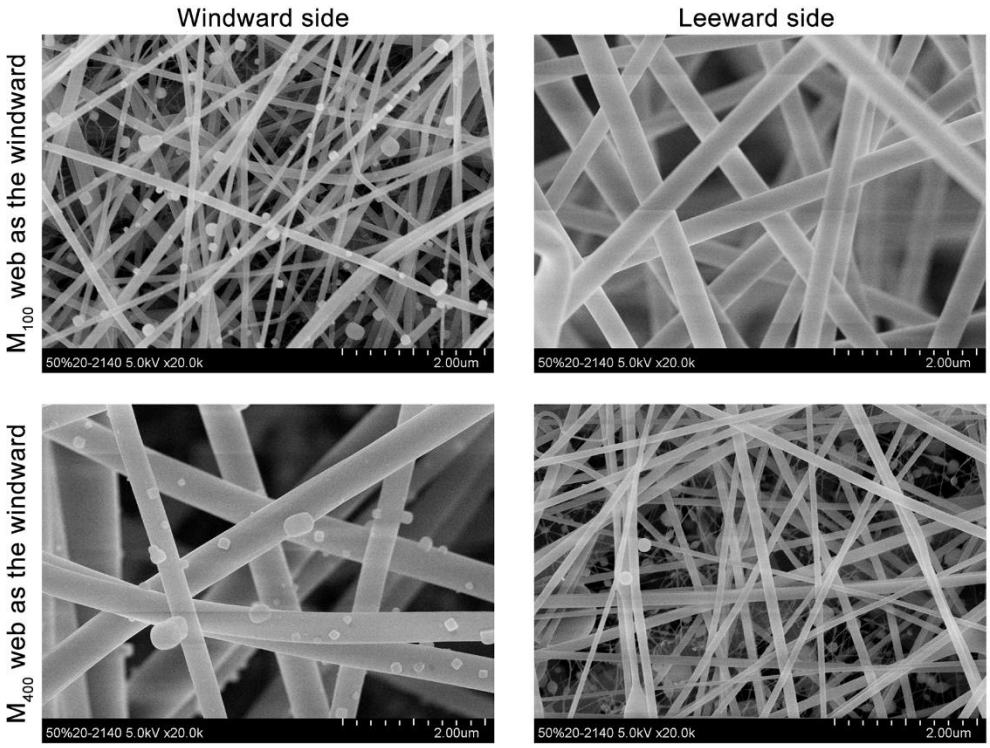

Supplementary Fig. 15 SEM images of M_{100}/H5/M_{400} web after filtration.

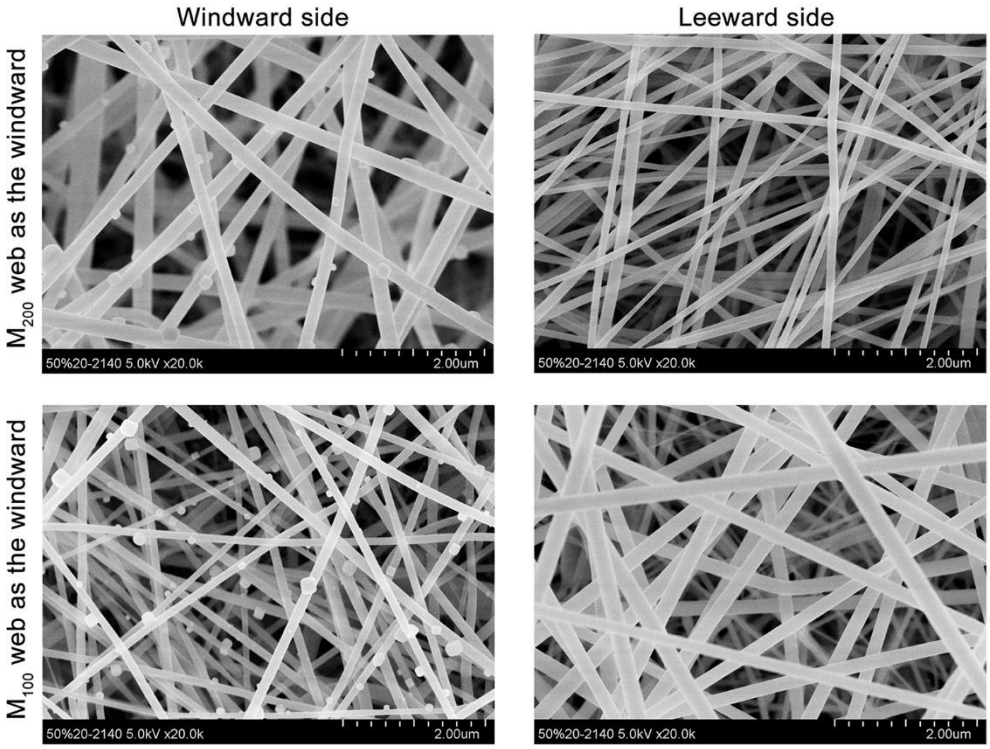

Supplementary Fig. 16 SEM images of M_{100}/H8/M_{200} sample after filtration.

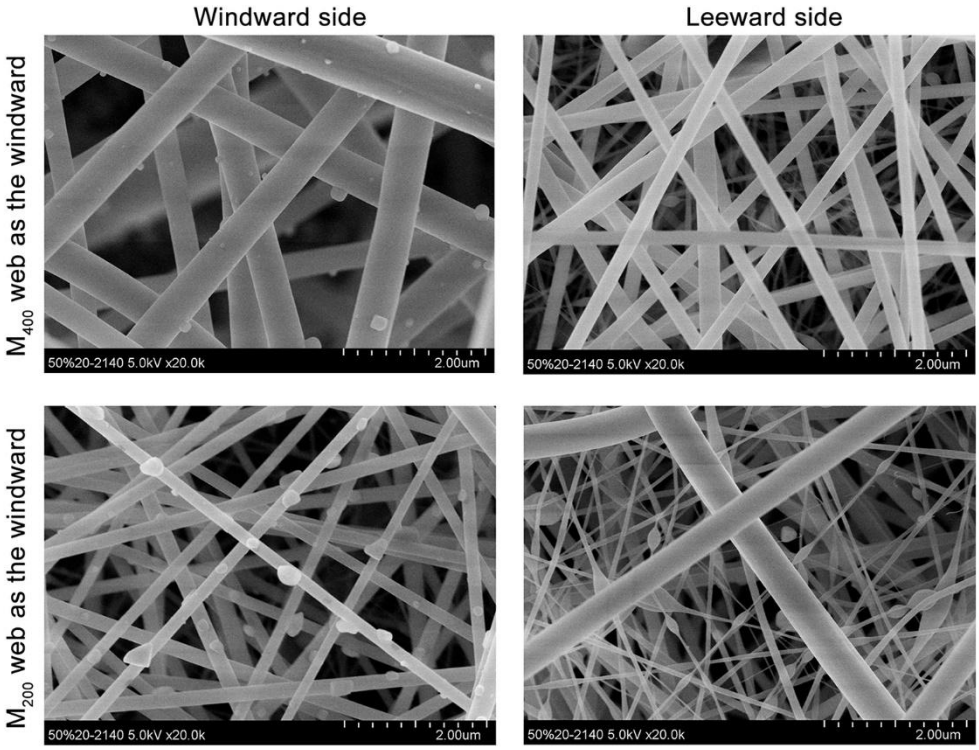

Supplementary Fig. 17 SEM images of M_{200}/H8/M_{400} web after filtration.

Supplementary Table 2. Performance comparison among our TSN filter, other electrospun fiber filters, and commercial filters.

Fiber filters	Average fiber diameter (nm)	Areal density (g m^{-2})	Mean pore size (μm)	Filtration efficiency (%)	Pressure drop (Pa)	Qf (Pa^{-1})	Airflow rate (cm s^{-1})	Ref.
Rod-zein fiber	120	12	/	99.9	1270	0.0054	4	[S3]
Ribbon-zein	2790	12		99.9	107	0.0645		
PVC/PU	960	21	3.524	99.5	144	0.0368	5.3	[S4]
TiO_2/PAN	900	/	1.9	97	145	0.0235	5.3	[S5]
PAN	300	75	2.93	99.984	174.5	0.05	3	[S6]
PLA bead-on-string	273.6	5.21	3.27	99.997	165.3	0.063	5.8	[S7]
PE/PA	126	/	6	92.68	54.8	0.048	5.3	[S8]
TPU	123	1	/	98.34	102.3	0.04	5.3	[S9]
PVDF/PAN	546/193	/	/	97.8	105	0.0365	/	[S10]
Glass fibers	930	50.8	/	99.829	266.56	0.0239	5.3	[S11]
Spunbond PA6/PE	17 μm	127	/	64.1	26.4	0.038	5.3	[S12]
Nano-meltblown PP	500	40	7.5	99.98	280	0.03	5.3	[S13]
Modified PP melt-blown	740	90	9.7	99.22	270	0.018	5.3	[S14]
TSN	400/20/200	0.88	0.8	99.92	89	0.08	5.3	**This work**

Supplementary Note 2

The numerical simulations of nanofiber filters' filtration performances were conducted to mimic the aerosol filtration test using COMSOL software.

- Geometry construction:

A 2D structural geometry was built vertically of isolated nanofibers with diameters of 420 nm, 20 nm, and 100 nm, respectively. A 2D assembly with multiple layered nanofiber webs was constructed, with diameters of 420 nm, 20 nm, and 100 nm for each web, respectively. A 3D integrated TSN structural geometry was built of two matrix webs (d_f: 420 nm and 100 nm) sandwiched with a hybrid web (micro-spheres and untralfine nanofibers (d_f: 20 nm)). Comparatively, coarse and fine nanofiber assemblies with fiber diameters of 420 and 100 nm were built in a single structure as the controls, with areal densities comparable to that of the integrated TSN geometry (0.45 g m^{-2}). To simplify calculations, the computational region was designed to be cylindrical with a diameter of 6 μm and a height of 9 μm.

- Simulation procedure:

To mimic the actual filtration test conditions, airflow with a velocity of 5.33 cm s^{-1} passes from the top layer as the inlet to the bottom as the outlet, carrying aerosols (solid rigid spheres) with a size of 0.26 μm. Additionally, the numerical simulations were performed based on an idealized model and a clean filter without clogging.[S15]

- Parameters:

The areal densities of the 3D filters were constructed with a similar value of 0.45 g m^{-2}. The porosity (ε) of filters was calculated via equation (S2):

$$\varepsilon = (1 - \varphi) * 100\% = (1 - \mathrm{V_f}/\mathrm{V}) * 100\% \quad \text{(S2)}$$

Where φ represents the solid volume fraction of filter, V_f denotes as volume of nanofibers, and V is the total volume of the filter. The air resistance (ΔP) is equal to the difference between the pressure of the airflow passing through the upper surface (P_{up}) and the lower surface (P_{low}) of the calculation domain, expressed as a formula: $\Delta P = P_{up} - P_{low}$. P_{up} and P_{low} values were directly derived after simulation calculations, respectively. The filtration efficiency (η) was obtained by the equation: $\eta = (1 - \eta_{low}) * 100\%$, where η_{low} represents the penetration rate of particles on the outlet layer and is obtained via the simulation calculation.

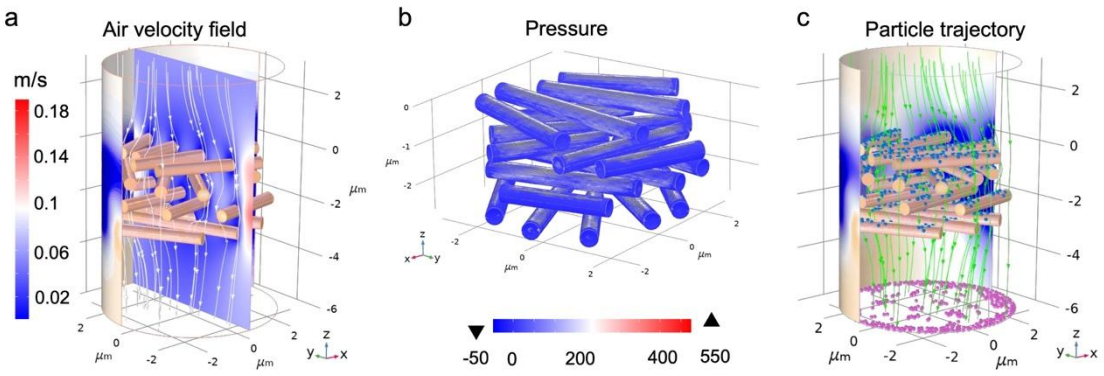

Supplementary Fig. 18 Simulation results of air velocity (a), pressure (b), and particle trajectory (c) for 420 nm dense assembly.

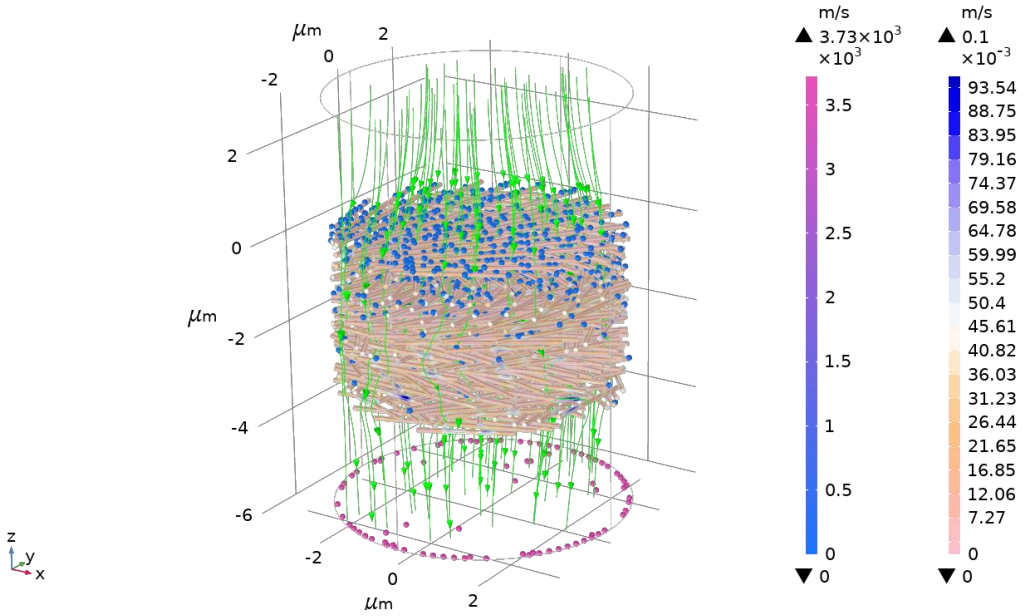

Supplementary Fig. 19 Simulation result of particle trajectory for 100 nm dense assembly.

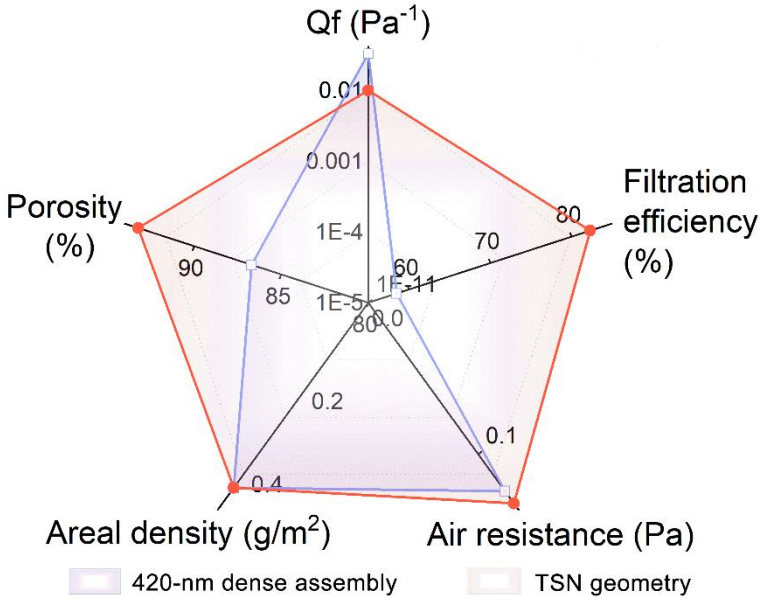

Supplementary Fig. 20 Simulation result of properties for the TSN geometry and 420 nm dense assembly.

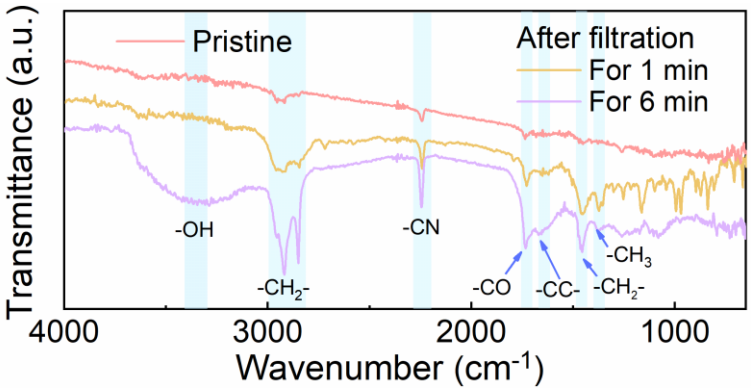

Supplementary Fig. 21 FTIR curves of the TSN material before and after filtration.

The FTIR spectra reveals prominent peaks at 2852 cm^{-1} and 1650 cm^{-1}, attributed to the $-CH_2$ and -C=C- groups, respectively. In addition, a new broad peak at 3240 cm^{-1} appears, which is attributed to O–H stretching vibrations originating from the intercepted pollutants.

Supplementary Note 3

Antibacterial activity

The antibacterial activity of samples was assessed using the agar diffusion method with Escherichia coli (E. coli) and Staphylococcus aureus (S. aureus).[S16] Bacterial cultures stored at low temperatures were inoculated onto solid agar medium using an inoculation loop and incubated at 37°C for 24 hours. A colony from the "131" section was then transferred to 20 mL of nutrient broth and incubated in a shaker at 37°C for another 24 hours. The cultured bacteria were diluted with deionized water at a ratio of 1: 100 to achieve a concentration of ~10^7 CFU/mL. A volume of 0.25 mL of this bacterial suspension was evenly spread on nutrient agar. The samples to be tested (diameter: 7 mm) were placed on top, and the petri dishes were incubated at 37°C for 24 hours.

The quantitative detection of E. coli was conducted using the shake flask method, following the GB/T 20944.3-2008 standard.[S17] The bacterial culture method was consistent with that of the disk diffusion method. The bacterial nutrient broth was diluted 1:100 in fresh nutrient broth and further diluted 1: 100 in PBS buffer to achieve a concentration of 5×10^5 CFU/mL. Nine different mass gradients of samples were placed in sealed, breathable flasks containing 5 mL of the bacterial broth and incubated in a shaker at 37°C for 18 hours. After shaking, 0.1 mL of the bacterial broth, diluted 1: 100 in PBS buffer, was evenly spread on nutrient agar and incubated at 37°C for 24 hours. The antibacterial rate (AR) was obtained in the equation (S3):

$$AR = ((N_c - N_s)/N_c) \times 100\% \quad \text{(S3)}$$

Where N_c and N_s denote the number of colonies that developed on the control and sample nutrient agar plates, respectively.

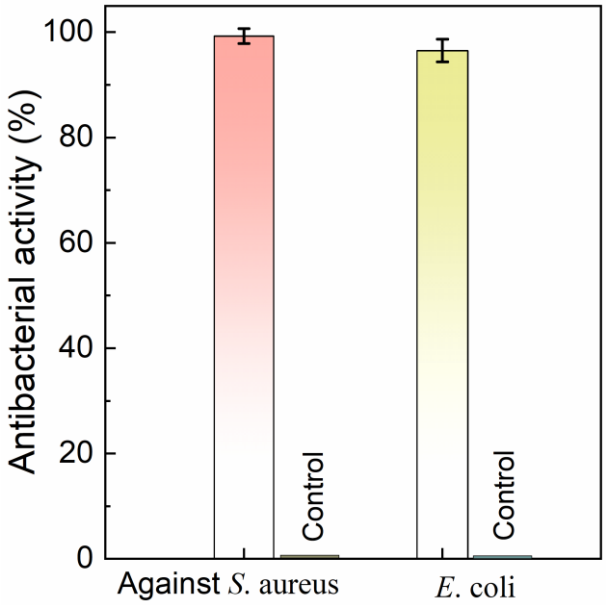

Supplementary Fig. 22 The antibacterial performance of the TSN@DTAC web.

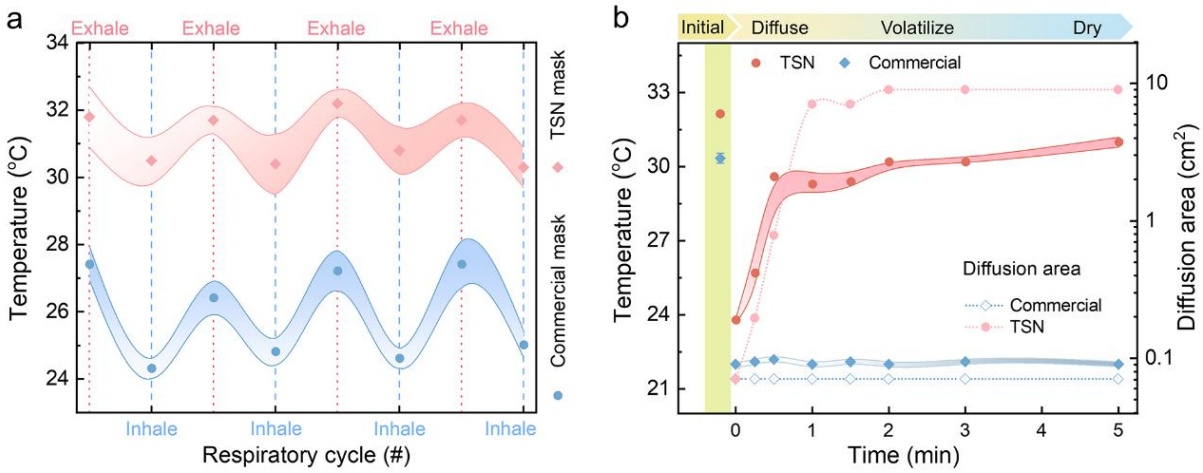

Supplementary Fig. 23 Surface temperature of TSN mask compared with commercial mask. a) During human inhaling and exhaling cycles. b) The water-sp[21]reading procedure on the surface of the mask filter elements.

During human respiratory activities, the surface temperature of our TSN-based mask increased from ~30.5 ºC to ~32 ºC (Figure S23a), whereas the temperature of a commercial mask fluctuated between ~24.7 ºC and ~27 ºC. These results demonstrate that the TSN filter, when used as a mask, can effectively dissipate heat, thereby maintaining thermal comfort for the wearer. Additionally, TSN web facilitates rapid spreading and evaporation of liquid water, which enhances wearing comfort (Figure S23b).

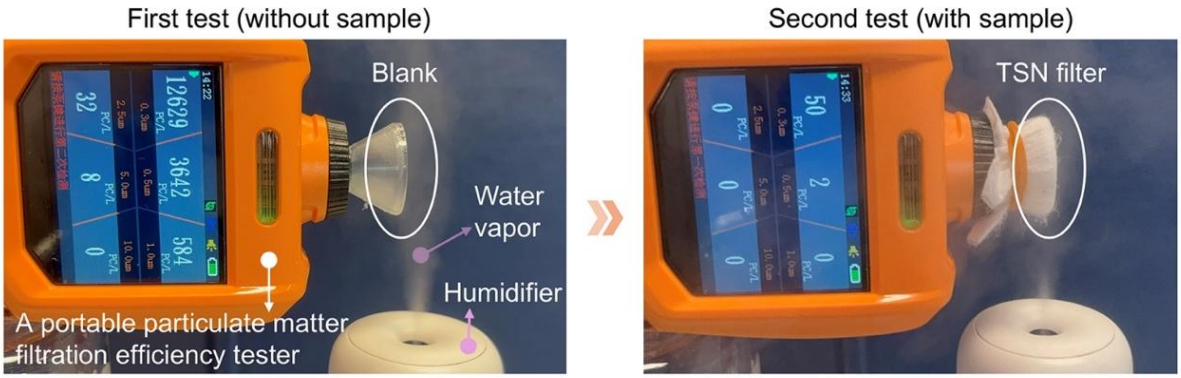

Supplementary Fig. 24 Demonstration of filtration performance test for TSN filter.

TSN filters prepared five years ago placed in a low-dust environment laboratory (Jan 2025, at HK) were measured with a portable particulate matter filtration efficiency tester (Model: HYX-MS600-6, SN: 23F27069, Guangdong Huiyixin Technology Co., Ltd. China). During the test, the samples were placed at the steam outlet of a humidifier, imitating humidity of human exhaled breath (Figure S25). Under high-humidity environment using a portable tester (Airflow velocity: 85 L/min).

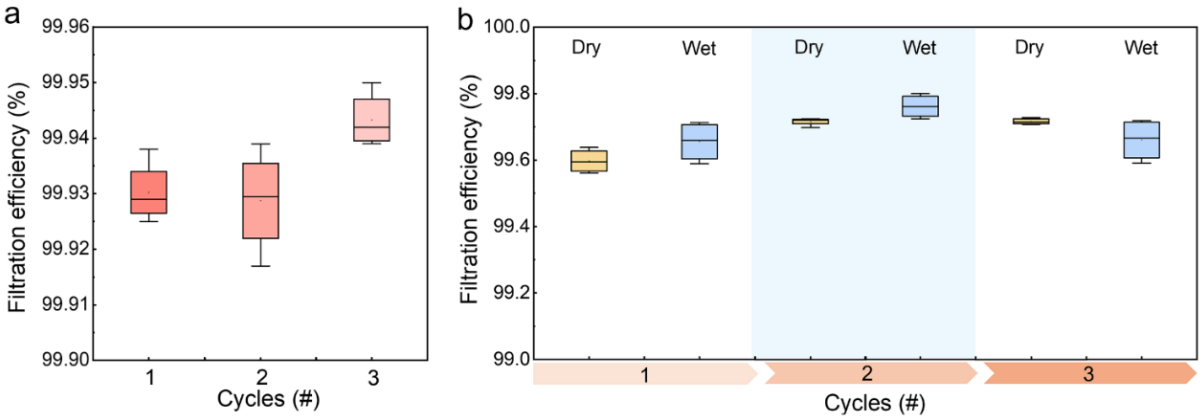

Supplementary Fig. 25 Filtration efficiency of TSN filters.

a) At high-humidity environment (~100%RH) for three cycles. b) Samples at dry and wet states under 45%RH for three cycles, respectively.

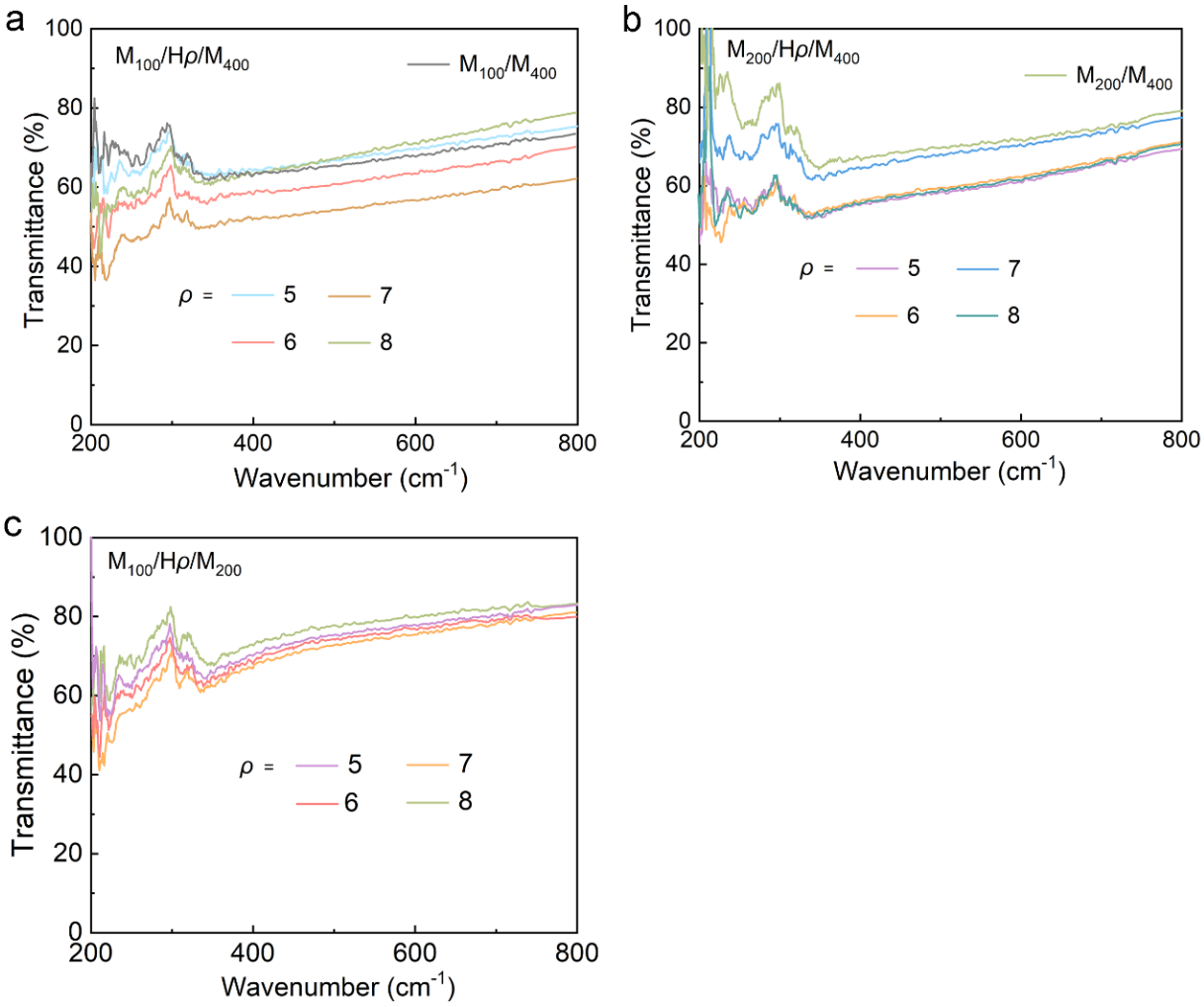

Supplementary Fig. 26 Transmittance of M100/Hρ/M400 (a), M200/Hρ/M400 (b), and M100/Hρ/M200 (c) webs in the visible light band.

Supplementary Movie 1. The dissolving procedure of a piece of TSN web disposal (Size: 4 × 4 cm^2) in two drops of solvent.

Supplementary Movie 2. Illustration of TSN filter for removal of aerosols in a dynamic filtration process.

Supplementary Movie 3. The dissolving process of plenty of TSN web disposal in solvent without greenhouse gas emissions.

References:

[S1] Xu J, Du X, Xin B, et al. Moisture-wicking and solar-heated coaxial fibers with a bark-like appearance for fabric comfort management[J]. ACS Appl Mater Interfaces, 2021, 13(22): 26590-26600.

[S2] Gennes P G, Brochard-Wyart F, Quéré D. Capillarity and wetting phenomena: drops, bubbles, pearls, waves.[M]//. Springer New York. 2004: pp 7-9.

[S3] Fan X, Wang Y, Zheng M, et al. Morphology engineering of protein fabrics for advanced and sustainable filtration[J]. Journal of Materials Chemistry A, 2018, 6(43): 21585-21595.

[S4] Wang N, Raza A, Si Y, et al. Tortuously structured polyvinyl chloride/polyurethane fibrous membranes for high-efficiency fine particulate filtration[J]. J Colloid Interface Sci, 2013, 398: 240-246.

[S5] Su J, Yang G, Cheng C, et al. Hierarchically structured TiO(2)/PAN nanofibrous membranes for high-efficiency air filtration and toluene degradation[J]. J Colloid Interface Sci, 2017, 507: 386-396.

[S6] Canalli Bortolassi A C, Guerra V G, Aguiar M L, et al. Composites based on nanoparticles and pan electrospun nanofiber membranes for air filtration and bacterial removal[J]. nanomaterials, 2019, 9(12): 1740.

[S7] Wang Z, Zhao C, Pan Z. Porous bead-on-string poly(lactic acid) fibrous membranes for air filtration[J]. J Colloid Interface Sci, 2015, 441: 121-129.

[S8] Xu Y, Zhang X, Hao X, et al. Micro/nanofibrous nonwovens with high filtration performance and radiative heat dissipation property for personal protective face mask[J]. Chem Eng J, 2021, 423: 130175.

[S9] Liu Y, Jia C, Li P, et al. Mass production of hierarchically designed engine-intake air filters by multinozzle electroblow spinning[J]. Nano Lett, 2022, 22(11): 4354-4361.

[S10] Jiang J, Shao Z, Wang X, et al. Three-dimensional composite electrospun nanofibrous membrane by multi-jet electrospinning with sheath gas for high-efficiency antibiosis air filtration[J]. Nanotechnology, 2021, 32(24).

[S11] Gao H, Yang Y, Akampumuza O, et al. A low filtration resistance three-dimensional composite membrane fabricated via free surface electrospinning for effective $PM_{2.5}$ capture[J]. Environmental Science: Nano, 2017, 4(4): 864-875.

[S12] Yeom B Y, Pourdeyhimi B. Aerosol filtration properties of PA6/PE islands-in-the-sea bicomponent spunbond web fibrillated by high-pressure water jets[J]. Journal of Materials Science, 2011, 46(17): 5761-5767.

[S13] Hassan M A, Yeom B Y, Wilkie A, et al. Fabrication of nanofiber meltblown membranes and their filtration properties[J]. Journal of Membrane Science, 2013, 427: 336-344.

[S14] Brochocka A, Majchrzycka K, K. M. Modified melt-blown nonwovens for respiratory protective devices against nanoparticles[J]. Fibres & Textiles in Eastern Europe, 2013, 21(4): 100.

[S15] Zhou M, Ma L, Zhou Z, et al. TriboNano shield–Scalable manufacturing anti-smog multi-level structured nanofiber air filter with co-enhanced purification performance towards self-powered window screen[J]. Nano Energy, 2024, 121: 109230.

[S16] Zhang H, Zhang T, Qiu Q, et al. Quaternary ammonium salt–modified polyacrylonitrile/polycaprolactone electrospun nanofibers with enhanced antibacterial properties[J]. Textile Research Journal, 2021, 91(19-20): 2194-2203.

[S17] GB/T 20944.3-2008. Textile—Evaluation for antibacterial activity—Part 3: Shake flask method.